Characterization of Magnetic Nanoscale Systems: From Molecules to Particles and Self-Assembled Chains

Bulbucan, Claudiu

2021

Document Version:
Publisher's PDF, also known as Version of record

Link to publication

Citation for published version (APA):
Bulbucan, C. (2021). *Characterization of Magnetic Nanoscale Systems: From Molecules to Particles and Self-Assembled Chains*. [Doctoral Thesis (compilation), Synchrotron Radiation Research]. Lund University.

Total number of authors:
1

General rights
Unless other specific re-use rights are stated the following general rights apply:
Copyright and moral rights for the publications made accessible in the public portal are retained by the authors and/or other copyright owners and it is a condition of accessing publications that users recognise and abide by the legal requirements associated with these rights.
- Users may download and print one copy of any publication from the public portal for the purpose of private study or research.
- You may not further distribute the material or use it for any profit-making activity or commercial gain
- You may freely distribute the URL identifying the publication in the public portal

Read more about Creative commons licenses: https://creativecommons.org/licenses/

Take down policy
If you believe that this document breaches copyright please contact us providing details, and we will remove access to the work immediately and investigate your claim.

LUND UNIVERSITY

PO Box 117
221 00 Lund
+46 46-222 00 00

Characterization of Magnetic Nanoscale Systems: From Molecules to Particles and Self-Assembled Chains

CLAUDIU BULBUCAN
DEPARTMENT OF PHYSICS | FACULTY OF SCIENCE | LUND UNIVERSITY

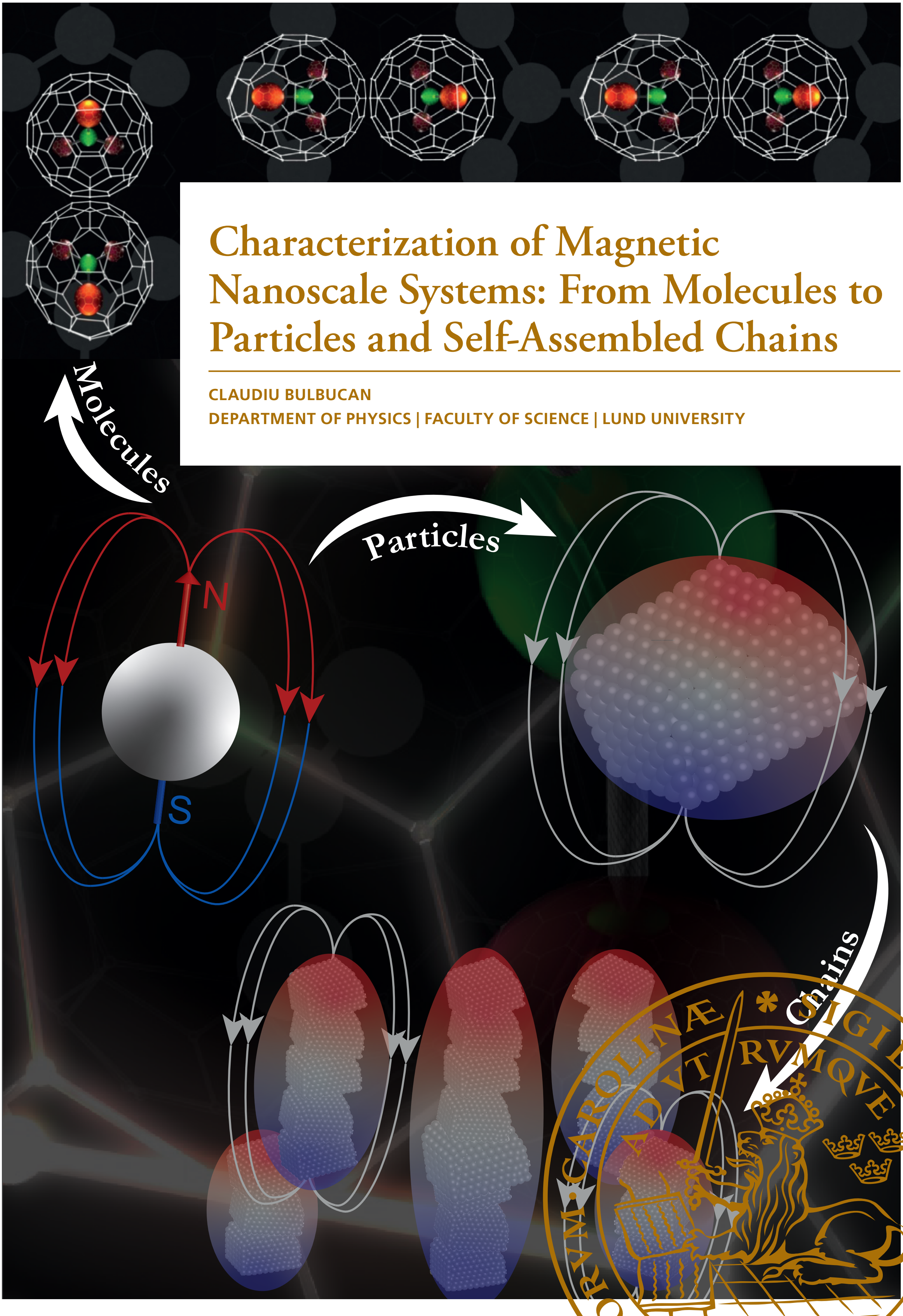
Molecules
Particles
N
S
Chains

Characterization of Magnetic Nanoscale Systems: From Molecules to Particles and Self-Assembled Chains

Characterization of Magnetic Nanoscale Systems: From Molecules to Particles and Self-Assembled Chains

by Claudiu Bulbucan

LUND
UNIVERSITY

Thesis for the degree of Doctor
Thesis advisor: Assistant Prof. Rasmus Westerström
Faculty opponent: Dr. Armin Kleibert

To be presented, with the permission of the Faculty of Science, Lund University, Sweden, for public criticism in Rydbergsalen at the Department of Physics on Friday, the 17th of December 2021 at 13:15.

DOKUMENTDATABLAD enl SIS 61 41 21

Organization
LUND UNIVERSITY
Division of Synchrotron Radiation Research
Box 124
SE–221 00 LUND
Sweden

Document name
DOCTORAL THESIS

Date of disputation
2021-12-17

Sponsoring organization

Author(s)
Claudiu Bulbucan

Title and subtitle
Characterization of Magnetic Nanoscale Systems: From Molecules to Particles and Self-Assembled Chains

Abstract

This thesis characterizes magnetic nanoscale systems with increasing size and aspect ratio using synchrotron radiation-based spectroscopy and microscopy techniques, combined with conventional magnetometry. The systems studied are molecular magnets, bimagnetic nanoparticles and self-assembled magnetic nanochains.

Single-molecule magnets are compounds that exhibit magnetic bistability and hysteresis at low temperatures. To investigate how their properties are affected when in contact with different surfaces, sub-monolayers of endofullerene $\mathrm{Dy_nSc_{3-n}N@C_{80}}$ ($n = 1, 2$) were prepared on conducting and insulating substrates by thermal evaporation and chemical deposition. In the latter case, the SMMs were functionalized with surface-anchoring thioether groups, which substantially affected the magnetic properties. However, magnetic hysteresis was observed on a surface of Au(111). The magnetic bistability was better preserved when sublimating the di-dysprosium compound ($n = 2$) onto Au(111), Ag(100), and MgO|Ag(100), exhibiting a wide substrate-independent hysteresis. While the magnetic bistability was unaffected, the orientation of the magnetic clusters was highly influenced by the choice of substrate.

Bimagnetic nanoparticles composed of two different magnetically ordered phases were synthesized by means of a spark ablation aerosol method. Cr substituted Fe-spinel oxide particles with embedded FeO subdomains with sizes of 10, 20 and 40 nm were investigated in detail. The unique structure was attributed to the presence of Cr and its influence on the oxidation of Fe. The 40 nm NPs exhibited a large exchange bias and an increase in coercivity when cooled in an applied field across the Néel temperature of FeO. The influence of particle size on the formation of the FeO subdomains, as well as the emergence of exchange bias were investigated and the results point to a decrease in the exchange field as the particle size decreases, with virtually no exchange bias present for the 10 nm system.

Nanochains were generated in a bottom-up approach by field-assisted self-assembly of aerosolized Co nanoparticles. Local magnetic properties were investigated by means of scanning transmission x-ray microscopy, complimented by micromagnetic simulations. While uniform chains have a single domain due to significant shape anisotropy, the inclusion of large multi-domain particles can facilitate domain-formation.

Key words

Magnetism, Magnetic Nanoparticles, Exchange Bias, Single Molecular Magnets, Magnetic Nanochains, X-ray Magnetic Circular Dichroism

Classification system and/or index terms (if any)

Supplementary bibliographical information

Language
English

ISSN and key title

ISBN
978-91-8039-110-8 (print)
978-91-8039-109-2 (pdf)

Recipient's notes

Number of pages
183

Price

Security classification

I, the undersigned, being the copyright owner of the abstract of the above-mentioned dissertation, hereby grant to all reference sources the permission to publish and disseminate the abstract of the above-mentioned dissertation.

Signature Claudiu Bulbucan

Date 2021-11-22

Characterization of Magnetic Nanoscale Systems: From Molecules to Particles and Self-Assembled Chains

by Claudiu Bulbucan

LUND
UNIVERSITY

Pages i to 66 © Claudiu Bulbucan

Paper I © The Royal Society of Chemistry 2018

Paper II © 1999-2021 John Wiley & Sons, Inc. All rights reserved

Paper III © 2019 American Chemical Society

Paper IV © The Royal Society of Chemistry 2021

Paper V © Manuscript

Paper VI © Manuscript

Cover illustration front: Magnetic atoms as a building blocks for molecular magnets, nanoparticles and nanochains.

Cover illustration back: Inside the C cage, by Rasmus Westerström.

Funding information: The thesis work was financially supported by the Swedish Research Council (grant 2020-005204) and the Skłodowska Curie Actions co-founding project INCA 600398.

© Claudiu Bulbucan 2021

Division of Synchrotron Radiation Research, Faculty of Science, Lund University, Sweden

ISBN: 978-91-8039-110-8 (print)
ISBN: 978-91-8039-109-2 (pdf)

Printed in Sweden by Media-Tryck, Lund University, Lund 2021

NORDIC SWAN ECOLABEL
Printed matter
3041 0903

Media-Tryck is a Nordic Swan Ecolabel
certified provider of printed material.
Read more about our environmental
work at www.mediatryck.lu.se

MADE IN SWEDEN 🇸🇪

TO DELIA

Contents

List of publications iii
Abstract v
Acknowledgements vi
Popular science summary vii
Abbreviations x

Characterization of Magnetic Nanoscale Systems: From Molecules to Particles and Self-Assembled Chains 1

1 Introduction 3

2 Fundamentals of magnetism 7
  2.1 Origins of magnetism 7
    2.1.1 Single atom 7
      2.1.1.1 Orbital and spin moments 7
      2.1.1.2 Spin-orbit coupling and Hund's rules 9
      2.1.1.3 Zeeman interaction 10
    2.1.2 Multiple atoms 11
      2.1.2.1 Magnetization and paramagnetism 11
      2.1.2.2 Exchange interaction 11
      2.1.2.3 Anisotropy 14
  2.2 Nanomagnetism 16
    2.2.1 Magnetic nanoparticles and superparamagnetism 16
    2.2.2 Single-molecule magnets 18
    2.2.3 Single and multi-domain nanoparticles 20
      2.2.3.1 Dipole-dipole interaction and the self-assembly of magnetic nanoparticles 22
    2.2.4 Exchange bias 23

3 Experimental techniques 27
  3.1 Electron microscopy 27
    3.1.1 Scanning Electron Microscopy 28
    3.1.2 Transmission Electron Microscopy 29
    3.1.3 Energy Dispersive X-ray Spectroscopy 30

3.2 X-ray based techniques 31
  3.2.1 Light-matter interaction 31
  3.2.2 Synchrotron radiation 33
  3.2.3 X-ray Diffraction 35
  3.2.4 X-ray Photoelectron Spectroscopy 37
  3.2.5 X-ray Absorption 38
  3.2.6 X-ray Magnetic Circular Dichroism 39
  3.2.7 Simulations 42
  3.2.8 Scanning Transmission X-ray Microscopy 42
  3.2.9 X-ray Photoemission Electron Microscopy 44
3.3 Magnetometry 45
  3.3.1 SQUID 45

4 Summary of papers **49**

5 Conclusions and outlook **53**

References **57**

Scientific publications **65**
5.1 Author contributions 65
Paper I: Magnetic hysteresis in self-assembled monolayers of Dy-fullerene single molecule magnets on gold 67
Paper II: Substrate-Independent Magnetic Bistability in Monolayers of the Single-Molecule Magnet Dy$_2$ScN@C$_{80}$ on Metals and Insulators . . 93
Paper III: Controlled Oxidation and Self-Passivation of Bimetallic Magnetic FeCr and FeMn Aerosol Nanoparticles 121
Paper IV: Large exchange bias in Cr substituted Fe$_3$O$_4$ nanoparticles with FeO subdomains 135
Paper V: Cr-substituted Fe$_3$O$_4$ nanoparticles: The role of particle size on the formation of Fe$_x$O subdomains and the emergence of exchange bias 149
Paper VI: Nanoscale X-ray Study of Self-Assembled Magnetic Nanochains . 159

List of publications

This thesis is based on the following publications, referred to by their Roman numerals:

I **Magnetic hysteresis in self-assembled monolayers of Dy-fullerene single molecule magnets on gold**
C. -H. Chen, D.S. Krylov, S. M. Advoshenko, F. Liu, L. Spree, R. Westerström, **C. Bulbucan**, M. Studniarek, J. Dreiser, A. U. B. Wolter, B. Büchner and A. A. Popov
Nanoscale, 2018, 24(10), pp. 11287–11292

II **Substrate-Independent Magnetic Bistability in Monolayers of the Single-Molecule Magnet $Dy_2ScN@C_{80}$ on Metals and Insulators**
D. S. Krylov, S. Schimmel, V. Dubrovin, F. Liu, T. T. N. Nguyen, L. Spree, C. Chen, G. Velkos, **C. Bulbucan**, R. Westerström, M. Studniarek, J. Dreiser, C. Hess, B. Büchner, S. M. Avdoshenko, A. A. Popov
Angewandte Chemie, 2020, 132(14), pp. 5805–5813

III **Controlled Oxidation and Self-Passivation of Bimetallic Magnetic FeCr and FeMn Aerosol Nanoparticles**
C. Preger, **C. Bulbucan**, B. O. Meuller, L. Ludvigsson, A. Kostanyan, M. Muntwiler, K. Deppert, R. Westerström, and M. E. Messing
The Journal of Physical Chemistry C, 2019, 123(26), pp. 16083–16090

IV **Large exchange bias in Cr substituted Fe_3O_4 nanoparticles with FeO subdomains**
C. Bulbucan, C. Preger, A. Kostanyan, K. M. Ø. Jensen, E. Kokkonen, C. Piamonteze, M. E. Messing and R. Westerström
Nanoscale, 2021, 22(24), pp. 13659-13665

V **Cr-substituted Fe_3O_4 nanoparticles: The role of particle size on the formation of Fe_xO subdomains and the emergence of exchange bias**
C. Bulbucan, P. Ternero, C. Preger, A. Kostanyan, M. E. Messing and R. Westerström
Manuscript

VI **Nanoscale X-ray Study of Self-Assembled Magnetic Nanochains**

C. Bulbucan, M. Sedrpooshan, C. Preger, S. Finizio, M. E. Messing and R. Westerström
Manuscript

All papers are reproduced with permission of their respective publishers.

Papers I have contributed to but are not included in this thesis:

VII **Magnetic microphase inhomogeneity as a thermodynamic precursor of ground-state phase separation in weakly coupled spin-$\frac{3}{2}$ chains**
L. Shen, E. Campillo, E. Young, **C. Bulbucan**, R. Westerström, M. Laver, P. J. Baker, and E. Blackburn
Phys. Rev. B, 103, 134420, 2021

VIII **Metamagnetic transition in monolayers of single-molecule magnet $Tb_2@C_{79}N$**
E. Koutsouflakis, D. Krylov, N. P. M. Bachellier, D. Sostina, V. Dubrovin, F. Liu, L. Spree, G. Velkos, S. Schimmel, Y. Wang, B. Büchner, R. Wetserström, **C. Bulbucan**, K. Kirkpatrick, M. K. Muntwiler, J. Dreiser, T. Greber, S. M. Avdoshenko, H. Dorn, A. A. Popov
Submitted manuscript

Abstract

This thesis characterizes magnetic nanoscale systems with increasing size and aspect ratio using synchrotron radiation-based spectroscopy and microscopy techniques, combined with conventional magnetometry. The systems studied are molecular magnets, bimagnetic nanoparticles and self-assembled magnetic nanochains.

Single-molecule magnets are compounds that exhibit magnetic bistability and hysteresis at low temperatures. To investigate how their properties are affected when in contact with different surfaces, sub-monolayers of endofullerene $\mathrm{Dy_nSc_{3-n}N@C_{80}}$ ($n = 1, 2$) were prepared on conducting and insulating substrates by thermal evaporation and chemical deposition. In the latter case, the SMMs were functionalized with surface-anchoring thioether groups, which substantially affected the magnetic properties. However, magnetic hysteresis was observed on a surface of Au(111). The magnetic bistability was better preserved when sublimating the di-dysprosium compound ($n = 2$) onto Au(111), Ag(100), and MgO|Ag(100), exhibiting a wide substrate-independent hysteresis. While the magnetic bistability was unaffected, the orientation of the magnetic clusters was highly influenced by the choice of substrate.

Bimagnetic nanoparticles composed of two different magnetically ordered phases were synthesized by means of a spark ablation aerosol method. Cr substituted Fe-spinel oxide particles with embedded FeO subdomains with sizes of 10, 20 and 40 nm were investigated in detail. The unique structure was attributed to the presence of Cr and its influence on the oxidation of Fe. The 40 nm NPs exhibited a large exchange bias and an increase in coercivity when cooled in an applied field across the Néel temperature of FeO. The influence of particle size on the formation of the FeO subdomains, as well as the emergence of exchange bias were investigated and the results point to a decrease in the exchange field as the particle size decreases, with virtually no exchange bias present for the 10 nm system.

Nanochains were generated in a bottom-up approach by field-assisted self-assembly of aerosolized Co nanoparticles. Local magnetic properties were investigated by means of scanning transmission x-ray microscopy, complimented by micromagnetic simulations. While uniform chains have a single domain due to significant shape anisotropy, the inclusion of large multi-domain particles can facilitate domain-formation.

Acknowledgements

This is dedicated to all the people who have helped me during my PhD studies. First and foremost, I would like to express my gratitude to my main supervisor Rasmus Westerström, who has provided constant support and guidance throughout this PhD and without whom none of this would have been possible. I would also like to thank my co-supervisor Maria Messing for the valuable comments, feedback and useful advice. I thank Calle Preger for providing the nanoparticles and nanochains I used in this work, along with helpful tips and comments.

I would also like to thank Cinthia Piamonteze for helping with the XMCD beamtimes, the data analysis and simulations. Thomas Greber is acknowledged for providing access to the SQUID and Aram Kostanyan for his support during the SQUID measurements and analysis tips. Furthermore, I would like to thank Alexey Popov and his group at IFW Dresden for the valuable discussions and tips during the XMCD beamtimes.

I would like to thank Mehran Sedrpooshan for his help with writing and micromagnetic simulations during the last stages of my thesis. Giulio D'Acunto is also acknowledged for helping out with the XPS analysis. I would like to thank Patrik Wirgin for helping out with the much feared administrative work, and also the fun discussions in the lunch room. Furthermore, I would like to thank all my colleagues at SLJUS for the friendly work environment, nice discussions and cool kick-off meetings.

This would have never been possible without the guidance and inspiration from my previous mentors, my MSc project supervisor Rami Sankari, my BSc supervisor Daniel Andreica and my high-school physics teacher Daniel Lazăr, whom I thank wholeheartedly.

Lastly, I would like to thank my family and friends for their love and constant support. Mom and dad, thank you for supporting me throughout this arduous journey. To my friends and godparents Irina and Mihai Pop, thank you for your constant support and also for keeping me honest. I thank my friends Raul Țifrea, Alex Macra and Alex Kelemen for their support and humorous distractions that were of great help to boost the mind. Furthermore, I am thankful to my new friends Payam Shayesteh and Mahsa Pezhman for their positive thoughts and input. Finally, I would like to thank my wife and better half Delia for her love and constant support throughout this journey.

Popular science summary

Magnetism is usually discovered during childhood when we find the intriguing attraction and repulsion between magnets. The first evidence of magnetism takes us back thousands of years to a region called Magnesia, located in Asia, where lodestone was magnetised by lightning strikes. Lodestone is a naturally occurring mineral composed of an iron oxide called magnetite (Fe_3O_4) which is, coincidentally, the main material used in the nanoparticles presented in this thesis. Although humanity did not understand the origin of the observed magnetic force, we were able to explore its uses intuitively in applications such as the compass. To make sense of the origin of magnetism, one has to go to the atomic level so the probability of reaching phenomena that cannot be approximated to everyday life increases significantly; therefore, as suggested by physicist Richard Feynman, we must find a common reference frame and allow for something to be true: I suggest that all atoms exhibit a form of magnetism, stemming from the circular motions of electrons like currents. In other words, each atom can be thought of as a small magnet. Since all matter is made up of atoms, how come not all materials are magnetic? Because, it is only for a few elements, such as iron and cobalt, that the small atomic magnets align rigorously so that the emerging magnetic force can be amplified and extends outside the material. For most elements, this force remains "hidden" within the material. It is not by far a complete model, but it will make do for the purpose of this section.

Magnets find applications in many technological areas, such as energy production, electric vehicles, speakers/headphones, computers, medical equipment and so on. Nowadays, with the ongoing miniaturization of devices, more and more interest has been switched to smaller size magnetism, usually referred to as nanomagnetism. The "nano" stems from a nanometer (10^{-9} m) and so nanoscale magnetism occurs typically on a $1 - 100$ nm length scale. At such small sizes, one is much closer to the "atomic magnets" previously mentioned than to the conventionally known everyday magnets. In this thesis, we have studied three different systems, namely single molecular magnets, magnetic nanoparticles and nanochains. Single molecular magnets are, with the exception of a single atom, the smallest magnetic units possible. Furthermore, the nanoparticles are "agglomerations" of atoms with sizes of several tens of nanometers. Lastly, the nanochains are composed of individual magnetic nanoparticles that merge together under their own magnetic attraction, helped by an applied field. At these dimensions, more interesting and even unexpected phenomena take place; rather than describing them in detail, I suggest we use their potential applications as motivation, such as high-density data storage. In 2015, the highest surface density in a hard disk drive was 1.34 Tbit/in^2 [1], translating into 1 $\text{bit}/481.5 \text{ nm}^2$. As such, we may imagine circular magnets with diameters of roughly 25 nm whose magnetization direction is used to encode binary information (e.g. "up" = 1 and "down"

= 0). However, using molecular magnets, the data density can be enhanced by one order of magnitude since their size is of the order of 1 nm.

It is also noteworthy to mention the investigative techniques used to study the small magnetic systems. Before going into details, I would like to ponder on the size difference between conventional macroscopic objects present into our daily lives, and nanoscale magnetic objects. Let us assume a 1.5 m tall person and a 1.5 nm molecular magnet. The difference in size is so staggering that it cannot be put into perspective with anything found on Earth, not even the Earth itself. If we consider the distance to the Moon of approximately $0.38 \cdot 10^9$ m ($\approx 380,000$ km), one would still need to cover it for four times to account for the equivalent size difference. As such, a great deal of finesse is required from the investigative techniques used throughout this work. In the 1800s, Michael Faraday observed that moving a magnet next to a conducting wire, a current is induced. The principle behind conventional magnetometry techniques is the same: the magnetic sample is moved in a controlled manner and its magnetic output induces a current that is amplified and read by computers. As expected for a nanoscale magnetic system, its magnetic output will also be very small; by cleverly exploiting quantum phenomena, the sensitivity of such a device can be high enough to detect even minute magnetic outputs, approximately 10^9 times weaker than the Earth's magnetic field. Furthermore, the magnetism of matter can also be probed with light, namely x-ray light, but to do so, a so-called synchrotron light source is needed, where the x-ray light is produced by high-energy electrons in a particle accelerator. These facilities are advantageous since the users have a great deal of control over the x-ray properties, such as energy (color) and polarization; the magnetic response of a sample can be investigated using a technique called x-ray magnetic circular dichroism, where x-rays of different ”colors” and polarizations are used. Moreover, for a magnetic material composed of more than one magnetic element, as opposed to a conventional magnetometry technique that measures everything in its sample chamber, circular dichroism can provide magnetic information from only one magnetic element because the ”color” of the x-rays is adjustable.

In this thesis, we have studied single molecule magnets on different substrates by means of magnetic circular dichroism and conventional magnetometry techniques. We have investigated their magnetic response as a function of applied field and temperature and saw that the substrate does not play a key role in the magnetic stability. However, the orientation of the molecular magnetic moments was highly influenced by the substrates used. Furthermore, we have investigated the magnetic properties of nanoparticles. The magnetic response here is given by three different iron ions, so using circular dichroism we could discern amongst them, and with the aid of computer simulations, we were able to calculate the concentration of each ion in the material. Furthermore, the nanoparticles are made up by two different magnetic materials, a

main one that occupies a larger volume proportion, and a much smaller one whose distribution may be imagined as the arrangement of raisins in a cake. The interaction between the two magnetic materials gives rise to new magnetic phenomena which we have investigated as a function of nanoparticle size using conventional magnetometry. Lastly, the nanochains were studied using ”microscopic” circular dichroism, where the x-rays are focused into a small spot, providing magnetic information from a small area the size of a nanoparticle. We found that the magnetic direction lies along the chains and reversing it by applying a field can more easily be accomplished in shorter chains or in the presence of a larger nanoparticle in the chain.

Abbreviations

- NP - Nanoparticle
- SMM - Single Molecular Magnet
- NC - Nanochain
- EB - Exchange Bias
- XMCD - X-ray Magnetic Circular Dichroism
- SQUID - Superconducting Quantum Interference Device
- VSM - Vibrating Sample Magnetometer
- XPS - X-ray Photoelectron Spectroscopy
- XAS - X-ray Absorption Spectroscopy
- XRD - X-ray Diffraction
- STXM - Scanning Transmission X-ray Microscopy
- XPEEM - X-ray Photoemission Electron Microscopy
- TEM - Transmission Electron Microscopy
- SEM - Scanning Electron Microscopy

Characterization of Magnetic Nanoscale Systems: From Molecules to Particles and Self-Assembled Chains

Chapter 1

Introduction

For millennia, the phenomenon of magnetism has intrigued humanity with its innate ability to cause remote attraction between certain materials. One such material is lodestone, which is a rock rich in Fe_3O_4 magnetite, a mineral magnetized by lightning strikes[2]. Although the first evidence dates back to ancient history, it was not until the early 19th century that scientists - such as Hans Christian Ørsted who discovered that a current running through a wire generates a magnetic field[3] and Michael Faraday who discovered electromagnetic induction[4] - started to diligently investigate magnetism and its connection to electricity, which subsequently paved the road towards significant achievements, such as electrification of the planet and intercontinental wireless communications.

An area of interest in the field of magnetism is represented by permanent magnets (PMs), materials capable of retaining magnetization even in the absence of an external magnetic field. Permanent magnets are integral parts of modern technologies such as mobile phones, computers, speakers, and medical equipment[5]. Sustaining the desired magnetic output from ever-decreasing permanent magnetic volumes is thus crucial for the miniaturization of electronic devices[6]. Moreover, permanent magnets are critical components in technologies that convert electric power into motion or vice versa, mechanical energy into electricity, and thus play a key role in replacing fossil fuel in vehicles and transitioning to renewable energy sources. A promising strategy for developing next-generation high-performing PMs is to combine microscopic structures of different magnetic materials using bottom-up approaches[5]. As such, there has been extensive focus on nanoscale magnetic objects in recent decades.

Nanomagnetism describes the magnetic behavior on the nanometer scale (10^{-9} m). Although it promises the development of new magnetic materials with increased performance, energy efficiency and reduced size, nanomagnetism is also important on a fundamental level, since the magnetic properties differ from their bulk counterparts. Importantly, the quantum nature of nanoscale systems opens the door to novel functionalities. For example, discovering the giant magnetoresistance effect (GMR)[7] in magnetic thin films paved the way for so-called spintronic devices that have revolutionized the field of magnetic memory applications[8]. This work focuses on three classes of nanomagnetic systems: molecular magnets, magnetic nanoparticles (NPs) and self-assembled magnetic nanochains (NCs).

In magnetic data storage, the binary information is encoded in the magnetization direction of small volumes within a magnetic material. Increasing the storage capacity thus entails decreasing the magnetic volume while maintaining a stable magnetization. The smallest conceivable magnetic unit would be that of a single atom or a small cluster of atoms. It has been demonstrated that the magnetic moment of a single Ho atom can be stabilized when adsorbed on an insulating MgO thin film[9], allowing for reading and writing information on a single-atom at sub-Kelvin temperatures[10]. However, atomic sub-monolayers are only stable under ultra-high vacuum conditions and an alternative approach is to stabilize a single or a pair of atomic magnetic moments inside a protective molecular cluster. Single-molecule magnets (SMMs)[11,12] are molecules exhibiting intrinsic magnetic bistability at low temperatures with a magnetization that can be stable on a sufficient timescale to be utilized in molecular spintronics[13] and qubits[14], and given a size of about 1 nm, they are promising candidates for high-density storage devices[15]. For the SMMs to be utilized in applications, they must be deposited onto a surface where the magnetic moments can be addressed and manipulated. Therefore, it is of interest to know how the magnetic properties are affected when they are removed from the bulk phase and assembled into low-dimensional structures on different substrates. A particularly promising class of SMMs for depositing onto surfaces are endofullerenes, where the magnetic clusters are protected inside a carbon cage, see figure 1.1 a). **Papers I** and **II** study the magnetic properties of sub-monolayers of endofullerene SMMs deposited onto conducting and insulating substrates. While the magnetic bistability is substrate-independent, the ordering of the molecular magnetic moments is strongly dependent on the surface.

Magnetic NPs with a size of about $5 - 100$ nm represent another important area of study in nanomagnetism. In particular, bimagnetic systems composed of two different magnetic phases can exhibit exchange bias (EB) effects which allows the magnetic properties be tailored for a wide range of applications such as high-density data storage[16], spintronics[17], biomedical[18,19,20], and rare-earth-free permanent magnet applications[21,22]. Bimagnetic NPs are commonly composed of two differently ordered magnetic phases in a core-shell structure and are generated using chemical synthesis based on the thermal decomposition of metal-containing precursors. While highly

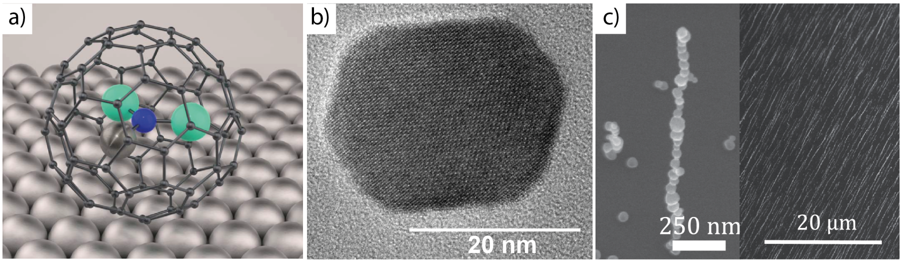

Figure 1.1: a) Schematic representation of a Dy_2ScNC_{80} single molecule magnet on a metal substrate; b) a transmission electron microscopy image of a FeCr-spinel oxide NP; c) a scanning electron microscopy images of Co self-assembled nanochains.

successful for generating monodispersed NPs with good control of the composition, chemical synthesis has drawbacks such as chemical waste, limitations in mixing different materials and the risk of introducing impurities during the generation process. A promising approach for generating NPs is found with aerosol techniques based on spark ablation. These techniques are continuous and scalable, provide good control of the size and composition, and the possibility of forming alloys of materials immiscible in bulk[23]. However, reports on complex mixed-metal magnetic nanoparticles using this approach are rather limited.

In **paper III**, we explore an aerosol technique based on spark ablation to generate mixed-metal magnetic NPs. Here the seed material for the NPs is evaporated in a spark discharge between two seed electrodes and transported away by a carrier gas, where the vapor condensates into sub-10 nm primary particles that form larger agglomerates as they collide. The agglomerates are given a known charge before being transported through a furnace where they are compacted at high temperatures, followed by size selection based on their electrical mobility. The charged NPs are finally deposited onto any substrate of choice using an electric field where they can be studied, see figure 1.1 b). We demonstrate that mixed-metal magnetic NPs can be generated with a transition-metal ratio almost identical to the seed materials. Moreover, by tuning the carrier gas, both metallic and oxide phases could be generated. By using stainless steel seed electrodes, novel bimagnetic NPs were synthesized, composed of a ferrimagnetic (FiM) $(Fe,Cr)_3O_4$ phase with antiferromagnetic (AFM) FeO subdomains exhibiting exceptionally large EB, as shown in **paper IV**. The formation of the unique bimagnetic structure was attributed to the generation process and the presence of Cr, which is known to significantly influence the oxidation of Fe. Also influencing the oxidation and magnetic phase composition is the particle size, and the effect of reducing the diameter on the formation of AFM subdomains and the emergence of EB was studied in **paper V**.

If the aerosolized NPs are deposited onto a substrate in the presence of an applied magnetic field, they self-assemble into one-dimensional structures, see figure 1.1 c). One-dimensional magnetic structures, such as NCs and nanowires, are recently attracting attention for maintaining significant shape anisotropy and high domain-wall velocities[24,25], making them suitable candidates for new devices based on domain-wall formation and motion[24,26]. Moreover, the magnetic properties and magneto-transport based on GMR are strongly size-dependent. The spark ablation technique in **papers III-V** provides excellent control of particle size and composition and thereby the possibility of tuning the self-assembled NCs' properties. An additional benefit for applications is that the NCs can be self-assembled onto any substrates, eliminating time-consuming and costly transfer steps. **Paper VI** describes an x-ray microscopy and micromagnetic simulation study of NCs composed of Co. The presented results indicate that larger particles along the NCs act as nucleation centers that facilitate domain formation.

The aim of this work is to provide the structural and magnetic characterization of the aforementioned nanoscale magnetic structures. As such, the theoretical concepts needed throughout this thesis, both fundamental and in connection to phenomena described in the papers, are presented in Chapter II. Moreover, the techniques utilized in this thesis are covered in Chapter III.

Chapter 2

Fundamentals of magnetism

2.1 Origins of magnetism

This chapter is aimed at introducing the reader to the magnetic concepts discussed throughout this work. It is divided into two main parts, namely the fundamentals of magnetism followed by magnetism at the nanoscale. The first part describes the origin of magnetism in matter, starting from the perspective of a single atom, moving towards macroscopic systems and the magnetic properties they entail. The second part discusses magnetism on the nanoscale and phenomena such as superparamagnetism, single and multi-domain nanoparticles and exchange bias. For an in depth description, the reader is referred to the book by J. Stöhr[27].

2.1.1 Single atom

2.1.1.1 Orbital and spin moments

As Hans Christian Ørsted discovered, a moving current in an enclosed loop gives rise to a magnetic dipole moment μ. For simplicity, let us consider a circular loop of area A and a current I; the generated magnetic dipole moment will then be:

$$\mu = IA \tag{2.1}$$

expressed in units of Am^2. This reasoning could be applied to the Bohr model of an atom where the electron orbits around the nucleus in circular paths, as illustrated in figure 2.1. Since a current is made up by electrons, its orbital motion will generate a magnetic dipole moment which is related to the electron's orbital angular momentum L by[28]:

$$\mu = -\frac{eL}{2m_e} \tag{2.2}$$

with m_e being the electron mass and $L = m_e v r$ the classical orbital angular momentum. In a quantum mechanical treatment, the quantity of interest is the projection $L_z = m_l \hbar$ along a quantization axis z, with m_l being the orbital magnetic quantum number. As such, substituting L in equation 2.2 we derive an expression for the orbital magnetic moment μ_L:

$$\mu_L = -\frac{e\hbar}{2m_e} m_l = -\mu_B m_l \tag{2.3}$$

where the quantity $\mu_B = \frac{e\hbar}{2m_e}$ is the Bohr magneton and it represents the elementary unit of electronic magnetic moment in an atom ($\mu_B \approx 9.274 \times 10^{-24}$ JT^{-1}). Because the current is flowing in an opposite direction to that of the electrons, the dipole moment is oriented anti-parallel to the orbital angular momentum vector (see figure 2.1).

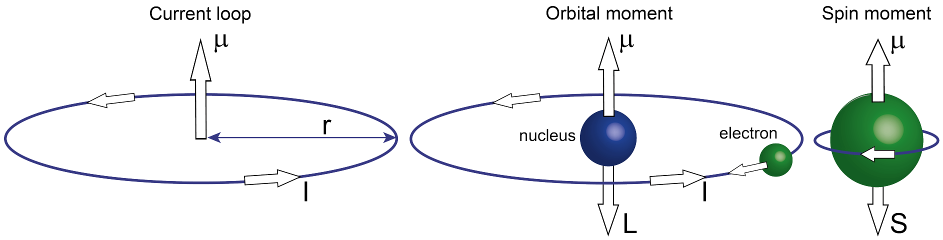

Figure 2.1: A loop of radius r with a circulating current I producing a magnetic moment μ oriented based on the right-hand rule; A schematic representation of the orbital angular momentum L as produced by the orbiting electron and the orbital moment μ; the spin orbital momentum S produced by the electron's intrinsic spin and charge properties, with the induced spin moment μ, illustrated intuitively as classical spin around its axis.

Furthermore, electrons posses an intrinsic orbital moment called spin, described by the spin quantum number $s = 1/2$. Its projection onto the quantization axis is then given by the spin magnetic quantum number $m_s = \pm 1/2$ corresponding to the "spin-up" and "spin-down" configurations. The spin magnetic moment is then given by:

$$\mu_s = -g_e \mu_B m_s \tag{2.4}$$

with $g_e \approx 2$ being the g-factor of the electron. Given the value of g_e and knowing that $m_s = \pm 1/2$, equation 2.4 shows that the magnitude of the spin magnetic moment of the electron is $1\ \mu_B$.

2.1.1.2 Spin-orbit coupling and Hund's rules

As previously discussed, a single electron's spin and orbital angular momenta give rise to spin and orbital magnetic moments. If the atom has more than one electron, L is now given by the sum of the individual electrons' orbital momenta; similarly, the individual spins combine yielding the total spin angular momentum S. These two momenta can interact with each other through the so-called spin-orbit (SO) coupling. The total atomic angular momentum is then given by equation 2.5 and the coupling scheme is known as Russel-Saunders coupling[29].

$$J = L + S \tag{2.5}$$

The lowest energy configuration of the electrons in a partially filled shell is given by Hund's rules[30]. The first rule dictates that the electrons maximize their total spin S due to Pauli's exclusion principle, which states that no two electrons can have the same quantum numbers. As such, electrons with the same spin avoid each other leading to a reduced Coulomb repulsion. Therefore, the electrons will firstly occupy one orbital each and only then start to pair with opposite spin electrons. Secondly, for a given spin configuration, the largest total orbital momentum L represents the lowest energy state. Qualitatively, this means that if electrons have a large total orbital momentum (i.e. they orbit in the same direction), it is less likely to meet in close proximity and so the repulsion is lower. Finally, for less than half-filled shells, the lowest energy configuration is achieved when the total angular momentum J is minimized, and thus $J = |L - S|$. Vice-versa, for a more than half-filled shell, $J = |L + S|$. The total atomic magnetic moment will then be given as a function of J. Similar to the orbital and spin magnetic moments, the total atomic moment is given as a function of the projection m_J of the total angular momentum along the quantization axis:

$$\mu_J = -g \mu_B m_J \tag{2.6}$$

where g is the Landé factor:

$$g_J = 1 + \frac{J(J+1) + S(S+1) - L(L+1)}{2J(J+1)} \tag{2.7}$$

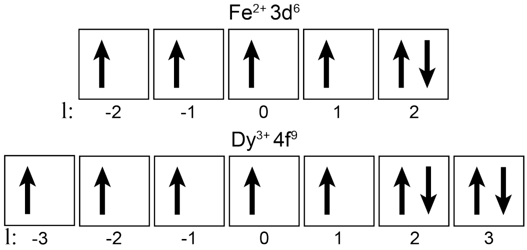

Figure 2.2: A schematic representation of the occupancy of the 3d orbitals for the Fe^{2+} transition metal ion and the 4f orbitals for the Dy^{3+} rare earth ion according to Hund's rules.

The nanoscale systems in this thesis contain trivalent magnetic $4f$ lanthanide ions and mixed-valence $3d$ transition metals. Applying Hund's rule to Dy^{3+} with a $4f^9$ valence gives a total orbital momentum $L = 5$ and total spin momentum $S = 5/2$. As such, the total angular momentum is $J = 15/2$, yielding a Landé factor $g_J = 20/15$ and hence, using equation 2.6, the atomic magnetic moment has a value of $10\ \mu_{\mathrm{B}}$, in good agreement with those measured in **paper II**. Moreover, it corresponds to the upper limit for μ_J, thus providing a scale for atomic moments ranging from $1\ \mu_{\mathrm{B}}$ to $10\ \mu_{\mathrm{B}}$. For the divalent transition metal ion Fe^{2+} with a $3d^6$ valence, the total spin momentum is $S = 2$ and the total orbital momentum is $L = 3$, giving a total angular momentum $J = 5$ and thus a Landé factor $g_J = 7/5$. As such, the expected magnetic moment is $\mu_J = 7\ \mu_{\mathrm{B}}$. However, the measured magnetic moment for the Fe^{2+} ion in Fe_3O_4 magnetite is $\mu_{\mathrm{measured}} = 5.4\ \mu_{\mathrm{B}}$[28]. The reason for the discrepancy is that Hund's rules do not necessarily predict the correct magnetic ground state as atoms come together to form molecules or solids. As we shall see in the coming sections, inter-atomic interactions are responsible for the magnetic properties typically associated with nanoscale and macroscopic systems. For the transition-metal ions, the spatially extended $3d$ wave functions interact strongly with the neighboring ions, resulting in a quenched orbital angular moment and an atomic magnetic moment primarily determined by the spin component. Thus, for the $3d$ systems in **papers III-VI**, spin and moment will be used interchangeably. In contrast, the localized $4f$ valence states interact weekly with the surrounding, preserving the atomic-like properties and an SO coupled Hund's ground state, allowing for stabilizing a single atomic moment in a molecular cluster, see section 2.2.2 and **papers I-II**.

2.1.1.3 Zeeman interaction

The interaction between the atomic magnetic moments μ and an externally applied magnetic field H is called the Zeeman interaction, and its energy can be expressed as follows[31]:

$$E_{Zeeman} = -\vec{\mu} \cdot \vec{H}\mu_0 = -\mu_J \mu_0 H \tag{2.8}$$

where H definex the quantization axis. The energy is thus minimized when the magnetic moments are aligned parallel to the field.

2.1.2 Multiple atoms

The origin of the atomic magnetic dipole moments was introduced so far. It is now of interest to study the behavior of atoms brought together to form a molecular cluster or a solid.

2.1.2.1 Magnetization and paramagnetism

The net magnetic moment per unit volume in such a system, given by the vectorial sum of the constituent atomic moments, defines the material's magnetization $\vec{M}$. With the exception of Fe, Co, and Ni, all elemental solids at room temperature exhibit null magnetization ($M = 0$) in the absence of an external field. Let us consider a system with N non-interacting atoms per unit volume, each with $J \neq 0$ and an atomic magnetic moment μ_{atomic}. In the absence of an external field, such a system exhibits no net magnetization due to thermal fluctuations (see figure 2.3 a)) .

The dependence of the magnetization with respect to an applied field is called a magnetization curve $M(H)$. For a paramagnet, applying a field causes the moments to align onto its direction as the Zeeman energy is minimized (see figure 2.3 b)). However, the thermal energy favors randomness and so the magnetization at a specific field is given by the equilibrium between the Zeeman and thermal energies. A paramagnet's magnetization curve is described by a Brillouin function, as shown in figure 2.3 d) for a given J at two temperatures. At high enough fields or sufficiently low temperatures, the Zeeman energy wins and the maximum magnetization $M_s = N \cdot \mu_{\text{atomic}}$, also known as the saturation magnetization, is reached (see figure 2.3 c)).

2.1.2.2 Exchange interaction

Conventionally, when we envision magnetism we think of permanent magnets. However, so far we have seen that a paramagnet has no magnetization without an applied field, although locally it has randomly oriented magnetic moments. Therefore, there must be some ordering of magnetic moments that leads to a non-zero magnetization even without a magnetic field. It is the exchange interaction that is responsible for

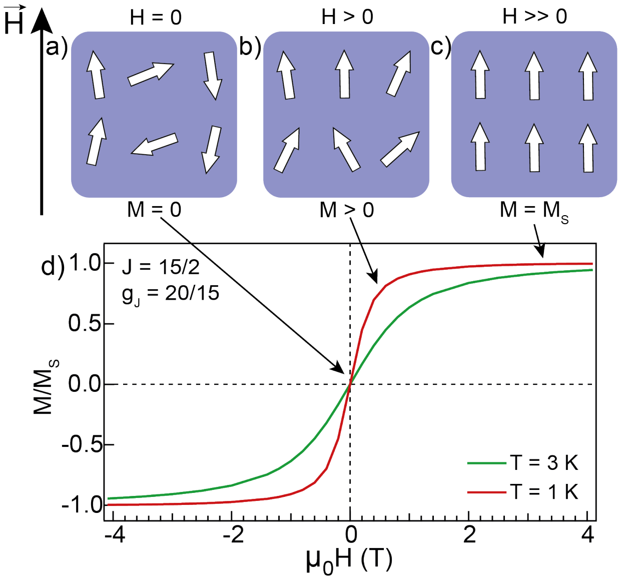

Figure 2.3: Magnetization under an externally applied magnetic field H: a) random orientation when the external field is zero with no net magnetization; b) partial orientation of the moments along the field direction with positive magnetization; c) all magnetic moments align with the field and the saturation magnetization is reached; d) two Brillouin functions plotted for two temperatures describing the paramagnetic behavior under an externally applied field. Both curves cross through zero at H = 0 as there is no magnetization in the absence of a field.

the magnetic ordering in matter. The exchange interaction between the electrons of two neighboring atoms, with spin configurations S_1 and S_2 can be described by the Heisenberg Hamiltonian[32]:

$$H_{spin} = -2j\vec{S_1} \cdot \vec{S_2} \tag{2.9}$$

where j is the exchange constant. Two cases may be discerned here, namely i) $j > 0$, which favors the parallel alignment of the spins, leading to a magnetic order called *ferromagnetism* (FM). In this case there is a net magnetization present even in the absence of an external magnetic field; ii) $j < 0$, which favors the anti-parallel alignment of the spins and so the material is termed an *antiferromagnet* (AFM) (see figure 2.4 a) and b)). Furthermore, if the opposing moments in an AFM have different magnitudes, the magnetic ordering is termed as *ferrimagnetism* (FiM) and it is sketched in figure 2.4 c).

As stated in section 2.1.2.1, the magnetic response of a paramagnet stems from the competition between the Zeeman energy that wants to align the magnetic moments with the applied field and the thermal energy, which favors randomness; in the absence of an external field, the thermal energy wins. However, for a magnetically ordered system, the competition will be carried out between the thermal and exchange energies. Therefore, we may define a transition temperature below which the exchange leads to magnetic ordering. For the ferromagnetic case, for example Co investigated in **paper VI**, the ordering temperature is called *Curie* temperature and it is $T_C = 1400$ K[33]; in the AFM case, example FeO in **papers IV-V**, the ordering temperature is the *Néel* temperature $T_N = 198$ K. Above these temperatures, both materials become paramagnetic.

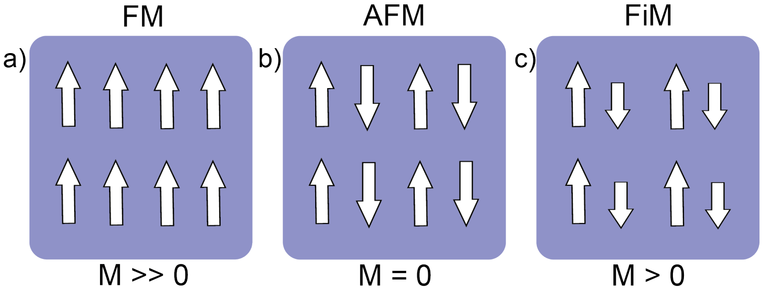

Figure 2.4: Atomic magnetic moments in magnetically ordered materials in the absence of an external field: a) ferromagnetic, b) antiferromagnetic and c) ferrimagnetic.

Magnetic ordering in elemental solids occurs due to the direct exchange between neighbouring atoms. However, in oxides, such as Fe_3O_4 and FeO studied in **papers IV** and V, the exchange is indirect and it is mediated through the O^{2-} atoms. The so-called *superexchange* is responsible for the AFM coupling between transition metal ions in the octahedral (B) and tetrahedral (A) sites of spinel oxides (see figure 2.5). Furthermore, *double exchange* leads to a FM coupling between the ions residing in the B sites of the spinel structure. In Fe_3O_4 (see figure 2.5), the AFM coupling occurs between the Fe^{3+} cations in the A and B sites, and so their magnetic moments cancel out, leaving the FM coupled Fe^{2+} as the sole contributor to the total magnetization. As such, the super and double exchange interactions are responsible for the FiM order in the material.

FM and FiM materials exhibit hysteresis below T_C in the field dependence of the magnetization. Figure 2.6 shows the magnetization curve recorded for Co NPs at a temperature of 2 K. The sample starts from an initial demagnetized state and its magnetization increases as a function of increasing the field H. As described in section 2.1.2.1, when the applied field is sufficiently strong, the magnetization may reach saturation M_S. The field is then reversed and, as it crosses the zero value, one notes a magnetization larger than zero. The magnetization value at zero field is called remanence magnetization M_R. As the field is further decreased, the magnetization decreases and switches its direction. The field at which the magnetization is zero is called the coercive field H_C and it is a measure of the system's reluctance towards demagnetization. The symmetric process happens in the negative side of the field.

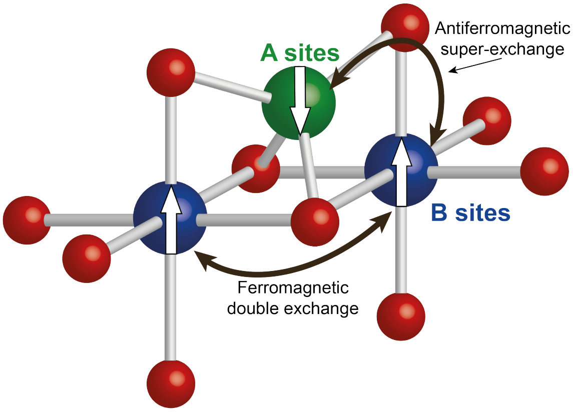
Antiferromagnetic super-exchange
A sites
B sites
Ferromagnetic double exchange

Figure 2.5: Magnetite spinel has an fcc-O lattice with tetrahedral (A) and octahedral (B) sites. The antiferromagnetic super-exchange ocurrs between the A and B sites (between the trivalent Fe ions) mediated by an oxygen ion, and the ferromagnetic double-exchange between the B sites of the spinel structure.

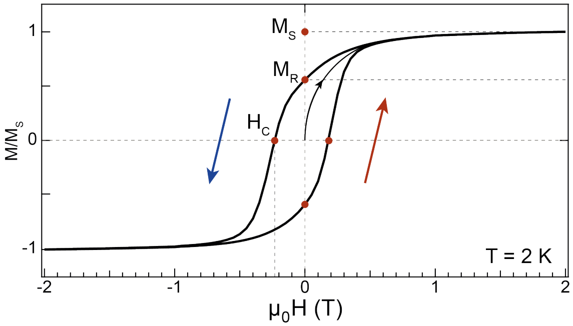

Figure 2.6: Hysteresis loop from Co nanoparticles. The data was recorded at a temperature of 2 K. The two arrows indicate the field sweeping direction and the red dots indicate the saturating M_S and remanence M_R magnetizations as well as the coercive field H_C.

2.1.2.3 Anisotropy

We now know exchange interaction between the electrons of neighboring atoms leads to a collective ordering of magnetic moments. However, the exchange interaction described by equation 2.9 is isotropic and does not favor the alignment along any particular direction and hence, would not lead to a stable magnetization. The preference to align atomic moments along specific directions is called magnetic anisotropy. The main contribution is typically magnetocrystalline anisotropy (MCA), which originates from the electrostatic interaction between the anisotropic charge distributions of atomic magnetic states with $L \neq 0$ and the neighboring ionic charges, referred to as crystal fields (CFs). Determined by the atomic states and the CF, the orbital magnetic moment will now have specific energetically favorable crystallographic directions called magnetic easy axes, to which the isotropic spin component can couple through the SO interaction.

A simple form of anisotropy is the uniaxial anisotropy with one easy axis, see figure 2.7. Switching between the two anti-parallel directions along the easy axis is associated with an anisotropy energy of $E_a = KV$[34], where K is the anisotropy constant [Jm^{-3}]. The anisotropy thus determines the coercivity, that is, the system's reluctance to change its magnetization direction. Since the magnitude depends on the SO coupling ($H_{SO} \propto \vec{L} \cdot \vec{S}$), the quenched orbital moment of $3d$ transition metals typically results in a lower MCA compared to the $4f$ systems. Conversely, the extended $3d$ wave functions are beneficial for the inter-atomic exchange coupling, thereby providing better resistance against thermal disorder, allowing the magnetic ordering to persist up to higher temperatures T_C than for systems with localized $4f$ states. The currently best performing permanent magnets NdFeB and SmCo combine $3d$ and $4f$ elements to achieve a large resistance towards demagnetization (i.e. a larger coercive field H_c) at reasonably high Curie temperatures T_C. The MCA is a local effect and can also be present in molecular clusters where it is typically referred to as single-ion anisotropy. Combining strongly SO coupled $4f$ lanthanide ions with suitable molecular CFs can stabilize a single atomic moment and produce magnetic hysteresis at low temperatures (see section 2.2.2).

Other types of magnetic anisotropy are shape anisotropy, where the shape of the material (such as thin films, nanowires or the nanochains investigated in **paper VI**) plays a role in creating easy axes. Inside the material, the magnetization generates a magnetic field H_d in the opposite direction, called the demagnetizing field. The simplest example is the case of a uniformly magnetized ellipsoid that has a demagnetizing field of the form $\vec{H_d} = -N_d\vec{M}$, with N_d being the demagnetizing factor and $\vec{M}$ the magnetization. The interaction between the magnetization and the demagnetizing field leads to the so-called magnetostatic energy, and for the ellipsoid it can be written as[35]:

$$E_{magnetostatic} \propto \int N_d M^2 dV \tag{2.10}$$

This relation is also approximately true for shapes that are limiting cases of an ellipsoid, such as thin films or wires. For a thin film, the demagnetizing factor N_d is null in-plane and positive out-of-plane, thus it is energetically favorable to have the magnetic moments in-plane. Similarly, for a wire or a nanochain, the shape anisotropy constrains the easy axes in plane such that the magnetization lies along the wire. However, in case of a sphere, $N_d = 1/3$ in any given direction, so there is no shape anisotropy present.

2.2 Nanomagnetism

The fundamentals of magnetism from a single atom to the collective ordering of many atoms were treated thus far. However, the aim of this work is to provide the characterization of magnetic nanoscale systems, motivated by the emergence of novel magnetic behavior at the nanoscale ($1 - 100$ nm). The systems investigated are single molecule magnets, magnetic nanoparticles and nanochains. This section introduces the reader to the fundamentals of nanoscale magnetism and relevant phenomena, such as superparamagnetism and exchange bias. For an in depth description, the reader is referred to the books of N. A. Spaldin[28] and A. P. Guimarães[36].

2.2.1 Magnetic nanoparticles and superparamagnetism

Let us consider a magnetically ordered particle with uniaxial anisotropy where all the atomic moments add up to a net magnetic moment, called "super spin", oriented along the easy axis. As described in section 2.1.2.3, the anisotropy energy depends on the anisotropy constant K and the volume V of the particle and generates a barrier ΔE associated with switching the magnetization direction along the easy axis (see figure 2.7).

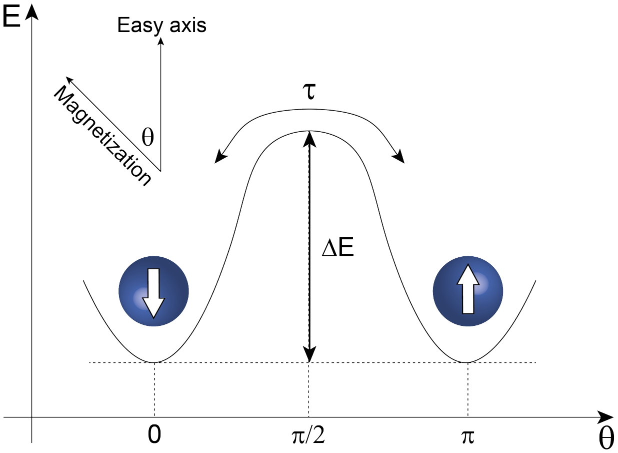

Figure 2.7: Uniaxial anisotropy where the anisotropy energy generated a barrier ΔE separating the two degenerate energy minima corresponding to the two anti-parallel directions along the magnetic easy axis .

As the particle volume decreases, the energy barrier ΔE becomes smaller, so the situation where the thermal energy $k_B T$ overcomes the anisotropy energy:

$$K \cdot V < k_B \cdot T \tag{2.11}$$

where k_B is Boltzmann's constant, can occur at temperatures well below room temperature. As such, the super spin can freely rotate about the magnetic easy axis and align along an applied magnetic field. However, in the absence of an applied field, the super spin fluctuations yield a null time-averaged magnetization. Thus, the super spin behaves similarly to a paramagnetic atom's magnetic moment, now with a magnitude given by the net magnetization of the whole particle volume (hence the term "super"); the phenomenon is known as superparamagnetism (SPM). The rate τ of fluctuation between the two directions set by the magnetic easy axis is given by the Néel expression[37]:

$$\tau = \tau_0 \exp\left(\frac{\Delta E}{k_B T}\right) \tag{2.12}$$

where $\Delta E = KV$ and τ_0 is the attempt frequency. As can be noted, the relaxation time scales exponentially with decreasing the temperature. Therefore, for a sufficiently low temperature, τ can become long compared to the measurement time. The system is then said to be in a blocked state since the magnetization appears static (frozen) on the time scale of the experiment.

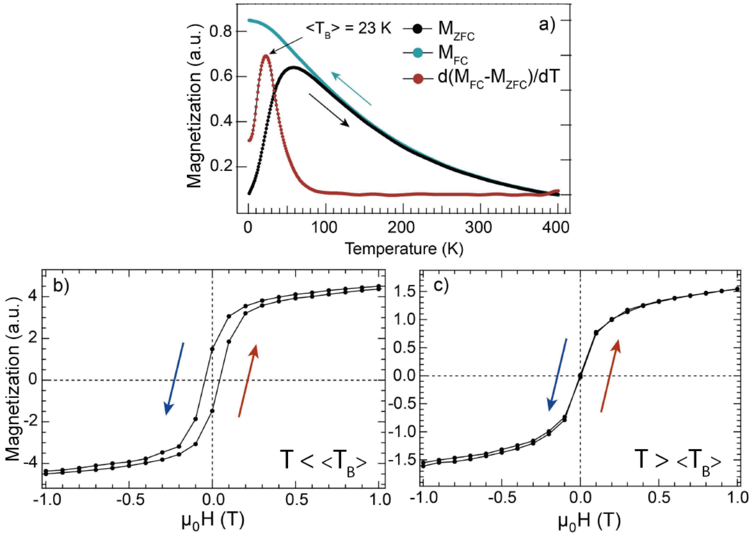

Figure 2.8: a) Temperature dependent magnetization of the 10 nm particles in the ZFC and FC protocols, along with the derivative of the two curves with respect to temperature. The arrows indicate the temperature sweep direction; Magnetization curves of the same systems recorded below the blocking temperature b) and above T_B c). The arrows here indicate the field sweep direction.

The transition between a blocked and an SPM state can be observed in temperature-dependent magnetization measurements. Figure 2.8 a) shows measurements from 10 nm FeCr-oxide NPs (**paper V**). The sample is firstly zero-field-cooled (ZFC) from 400 K to 2 K, leading to the super spins being randomly frozen along the magnetic easy axes as the relaxation rate τ decreases. At the start of the experiment, a small field of 10 mT is applied, and the magnetization is measured while heating. The system is initially in a blocked state with null magnetization, but as the temperature increases, the particle moments start aligning with the field as the increased thermal energy starts to overcome the anisotropy barrier ΔE, resulting in the noted increase in magnetization. At a certain temperature, the curve exhibits a maximum after which it merges with the magnetization M_{FC} measured while field-cooling (FC) under the same applied field. The subsequent decrease in magnetization is accounted for by the increased thermal energy that favors randomness with increasing the temperature. The reversible temperature range where the M_{ZFC} and M_{FC} curves overlap corresponds to the SPM state where the relaxation time is sufficiently short for the system to adopt an equilibrium magnetization determined by the thermal and Zeeman energies. Conversely, the irreversible low-temperature range is the blocked state where the differences between the M_{ZFC} and M_{FC} are related to the anisotropy of the system. For an ideal system of monodispersed and non-interacting particles, the maximum in the M_{ZFC} curve represents a transition temperature between the blocked and SPM states and it is referred to as the blocking temperature T_B. However, for a NP system with a finite size distribution, each particle would have a different anisotropy barrier KV and hence a different blocking temperature. The system would thus have a distribution of transition temperatures, and it has been suggested that the average blocking temperature <T_B> can be determined by performing the derivative of the difference of the two curves with respect to temperature $d(M_{FC} - M_{ZFC})/dT$[38], see figure 2.8 a).

The transition from an SPM to a blocked state also influences the field-dependent magnetization recorded at a constant temperature. Figure 2.8 b) and c) shows magnetization curves recorded below and above the blocking temperature from the 10 nm FeCr-spinel oxide NPs. As expected from a paramagnetic system, magnetization curves recorded at temperatures T > <T_B> do not show hysteresis. However, below <T_B> the system is in a blocked state and does not have time to reach an equilibrium magnetization as the magnetic field is varied, resulting in hysteresis.

2.2.2 Single-molecule magnets

The fullerene was discovered experimentally in 1985 by R. Smalley, R. Curl and H. Kroto at Rice University, Houston[39], and it was firstly named the "Buckminsterfullerene", after the American architect Buckminster Fuller. Sometime later, the nitride-cluster-fullerene $Sc_3N@C_{80}$[40] was discovered, paving the way for encapsulating magnetic clusters inside the C_{80} cage, which led to the discovery of endofullerene molecular magnets[41]. So-called single-molecule magnets (SMMs) are SPM molecules that exhibit a blocked magnetization with hysteresis below the blocking temperature, similar to the NPs in section 2.2.1. It should be noted that hysteresis is an intrinsic property of the molecules, resulting from single-ion anisotropy, and can be observed from compounds with only a single $4f$ magnetic ion. Thus, in contrast to the NPs, $4f$ SMMs do not rely on exchange interaction and magnetic ordering. However, it turns out that exchange interactions between two ions are beneficial, whereas adding more ions can make the magnetization less stable due to frustration[42]. Figure 2.9 shows a stick-and-ball schematic of the $Dy_nSc_{3-n}N@C_{80}$ $(n = 1-3)$ endofullerene SMMs and their corresponding hysteresis loops, illustrating the aforementioned effect of adding magnetic ions.

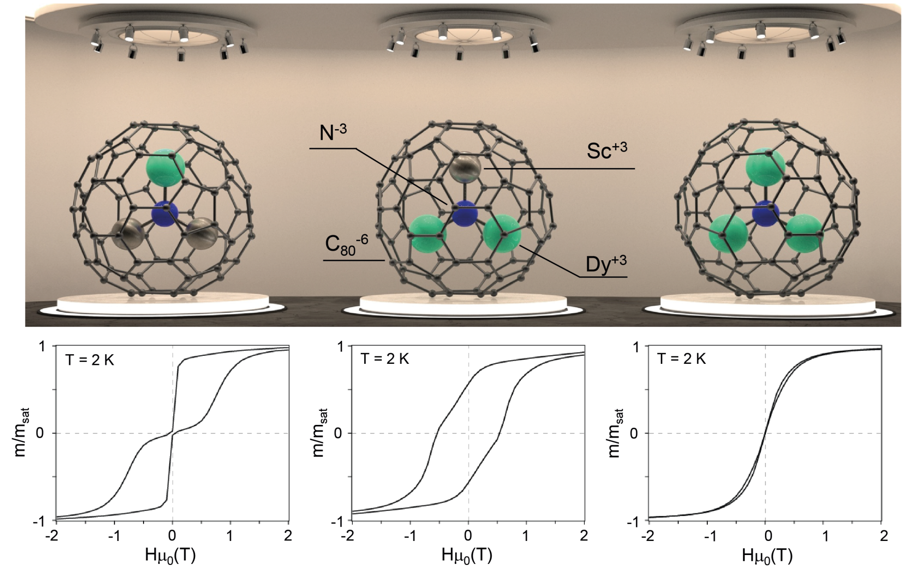

Figure 2.9: Stick-and-ball models of the three $Dy_nSc_{3-n}N@C_{80}$ fullerenes: left: n = 1, middle: n = 2 and right: n = 3, with their corresponding magnetization curves below.

The magnetic properties of sub-monolayers of the single-ion $(n = 1)$ and di - dysprosium compound $(n = 2)$ on different substrates were investigated in **papers I** and **II**. These systems are composed of a C_{80} cage with a triangular cluster made up of paramagnetic Dy^{3+} and diamagnetic Sc^{3+} ions at the corners of a triangle with a central N^{3-} ion (see figure 2.9). Interaction between the $4f$ valence orbitals and the CF, mainly from the central N^{3-} ion, stabilizes a $J_z = 15/2$ Hund's ground state (section 2.1.1.2) with a uniaxial anisotropy barrier ΔE and magnetic easy axes directed along the Dy-N bonds. The situation is identical to that of the SPM system in figure 2.7, where now the moments correspond to a single ($n = 1$) or two coupled ($n = 2$) trivalent Dy moments ($\mu = 10\ \mu_B$). As such, the relaxation rate τ is again given by equation 2.12, explaining the magnetic bistability and the observed hysteresis below T_B. Similar to the SPM particles, the system exhibits a paramagnetic behavior without hysteresis above T_B, see figure 2.10 a). However, in contrast to NPs, the magnetic moment of the single-ion magnet ($n = 1$) can shortcut the anisotropy barrier via quantum tunneling of the magnetization, which leads to a sharp decrease in the magnetization close to zero fields (figure 2.9 left-panel). This effect is suppressed for $n = 2$ due to an indirect exchange interactions between the Dy moments, stabilizing the remanent magnetization at temperatures below the blocking temperature, as shown in the middle-panel of figure 2.9.

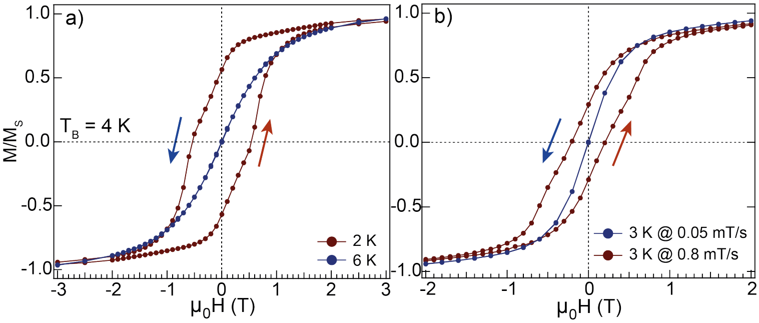

Figure 2.10: a) Magnetization curves at 2 and 6 K from $Dy_2ScN@C_{80}$ molecular magnets. As can be noted, at 2 K the system is in a blocked state exhibiting both coercivity and remanence; however, at 6 K, the behavior is paramagnetic; b) magnetization curves at 3 K recorded with two different field sweep rates. For the 0.8 mT/s case, the system exhibits a blocked state behavior whereas for a much slower sweep rate (0.05 mT/s), the magnetization has time to relax, exhibiting a paramagnetic behavior. The arrows indicate the field sweep direction. .

It should be emphasized again that the blocking temperature depends on the measurement and it is thus not an intrinsic property of the system. A system is said to be in a blocked state if the relaxation rate given by equation 2.12 is slow compared to the measurement time. This was illustrated in figure 2.10 b), where magnetization curves from $Dy_2ScN@C_{80}$ SMMs were recorded at a constant temperature of 3 K, but with significantly different field sweep rates (measurement times). Hysteresis is again observed for the faster measurement times. However, for the slower field sweep rates, the system has time to reach equilibrium, and the magnetization curve now has a shape expected from a paramagnet.

2.2.3 Single and multi-domain nanoparticles

For the NP systems, if the volume is sufficiently large, the anisotropy energy overcomes the thermal fluctuations at a given temperature and a stable magnetization within a single domain can be formed. We now know the exchange interaction is responsible for the parallel alignment of magnetic moments onto a direction given by the MCA. Hence, we would expect that a FM or FiM material should have all its constituent moments aligned parallel throughout its entire volume, or, in other words, in a single domain, thus minimizing its total exchange energy. However, the exchange energy is not the sole contributor to the total magnetic energy of a FM or FiM, but merely a component. Another main component of the total magnetic energy is the magnetostatic energy, described by equation 2.10.

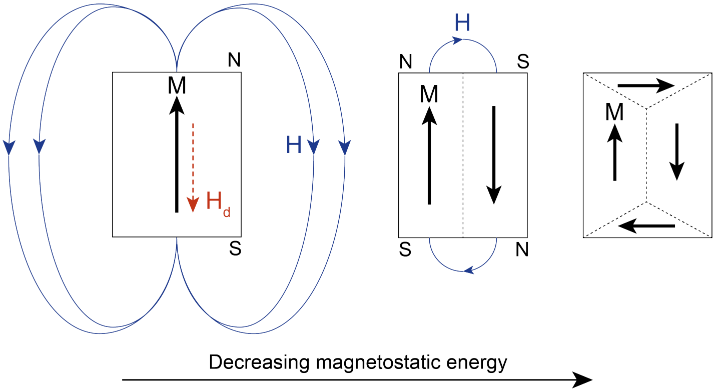

Figure 2.11: An example of magnetic domain formation that reduces the magnetostatic energy. As can be noted, from left to right, the intensity of the magnetic field lines decreases with adding more domains with anti-parallel and orthogonal magnetization orientations.

Figure 2.11 a) shows a single magnetic domain that has a macroscopic magnetization, creating an external field. As mentioned in section 2.1.2.3, since the field is oriented anti-parallel with respect to the magnetization, it is referred to as the demagnetizing field H_d. It is the demagnetizing field that creates the magnetostatic energy, which is responsible with the magnetic interactions between e.g. two magnetic blocks. The magnetostatic energy can be decreased by the formation of multiple magnetic domains (see figure 2.11 b) and c)), which reduces the demagnetizing field. However, forming anti-parallel magnetic domains entails an increase in exchange energy due to the anti-parallel orientation of neighboring spins. This is overcome by having larger so-called domain walls, which may be imagined as ”transition zones” between the two magnetic domains, such that the anti-parallel orientation is accomplished gradually. However, this leads to an increase in the anisotropy energy, since it prefers the moments be aligned along the easy axes. Therefore, the domain wall width will be determined by a compromise between the anisotropy and exchange energies, encompassed into the domain wall energy. As such, in a magnetic NP, the contest lies between the magnetostatic and domain wall energies. The magnetostatic energy is volume dependent (R^3 - with R the spherical particle radius) whilst the domain wall energy is surface dependent (R^2). Therefore, there exists a critical radius R_c below which it is more favorable to have a single domain (see figure 2.12).

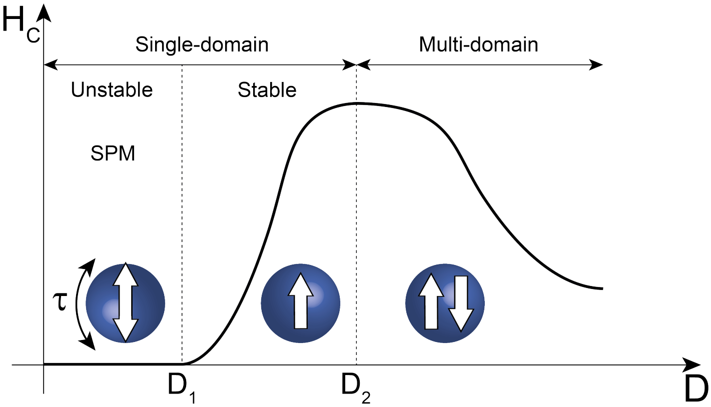

Figure 2.12: The dependence of coercive field with particle diameter. As can be noted, the particles may have single or multi-domains and the critical diameter is denoted as D_2. Furthermore, the single-domain particles may be stable or unstable, and the critical diameter between an SPM and single-domain is marked by D_1.

2.2.3.1 Dipole-dipole interaction and the self-assembly of magnetic nanoparticles

In a single-domain NP, the constituent atomic magnetic moments will add up to a large dipole moment, and so it may prove useful to envision each particle as a large dipole moment. The atomic dipole moment creates a magnetic field such as sketched in figure 2.13. This field will act on other dipoles and such an interaction gives rise to a force which tends to align the dipoles with the direction of the magnetic field. Moreover, the magnetic dipoles attract each other, which is the reason behind the self-assembly of the Co nano-chains presented in **paper VI**.

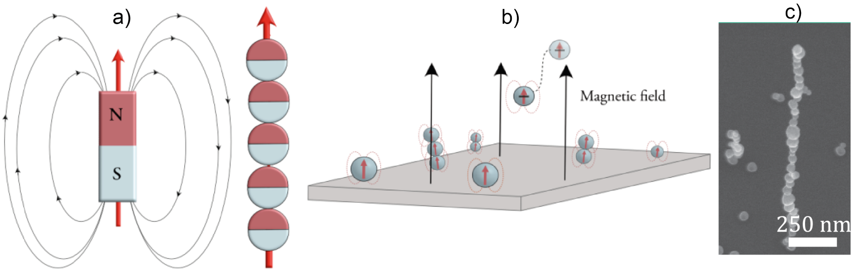

Figure 2.13: a) The magnetic field lines produced by a magnetic dipole along with magnetic nanoparticles self-assembling into nano-chains due to dipolar magnetic attraction; b) a schematic of the deposition procedure where the magnetic field is applied out-of-plane to guide the self-assembly; c) an SEM image of the resulting NC. The nanoparticles here are considered small individual dipoles. Picture courtesy of Calle Preger.

2.2.4 Exchange bias

We have studied bimagnetic NPs composed of two different magnetic phases, where the emergence of exchange bias (EB) is of particular interest. The presence of EB requires that a fixed (rigid) phase be exchange coupled with a reversible FM/FiM phase. Commonly, the fixed phase is an AFM with a high anisotropy, but it could also be e.g. frozen surface spins at low temperatures (small and hollow NPs[43]). If the system is cooled in an applied magnetic field through the Néel temperature of the AFM phase (here $T_C > T_N$), the exchange coupling at the interface can induce a unidirectional anisotropy, resulting in the shift of the hysteresis loop with respect to the field axis. In this thesis, EB was studied in the Cr substituted Fe-spinel oxide bimagnetic NP systems described in **papers III-V**. The synthesis method allowed for a unique structure of a host FeCr-spinel (FiM) with embedded Fe_xO (AFM) subdomains (as shown in figure 2.14), thus creating a large interface area between the two magnetic phases. For the 40 nm NPs characterized in **paper IV**, a large EB of $\mu_0 H = 460$ mT was found. Moreover, **paper V** describes the dependence of the EB and coercivity with the cooling field and temperature for three different particle sizes (10, 20 and 40 nm).

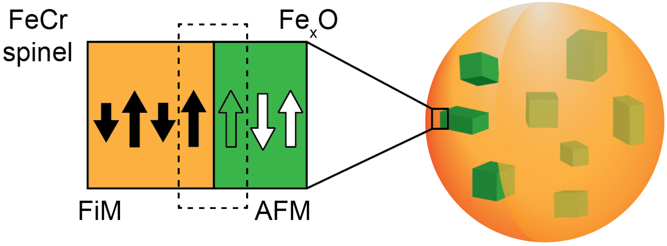

Figure 2.14: The host spinel structure (orange) of the Cr substituted Fe-oxide NPs with embedded rock-salt subdomains (green), with an illustration of the magnetic moments at the interface between the two magnetic phases.

Although a clear microscopic model for EB has yet to emerge[44], a qualitative understanding of the phenomenon may be derived from the intuitive spin configurations at the FiM (FM)/AFM interface, as shown schematically in figure 2.15. As the host spinel phase of the systems in **papers IV** and **V** is FiM, the description will be provided using FiM as a reversible phase. Assuming the Néel temperature smaller than the Curie temperature, applying a field between the two temperatures (i.e. $T_N < T < T_C$), the FiM moments align along the direction of said field. Cooling down through the Néel temperature prompts the magnetic ordering of the AFM phase, resulting in the parallel coupling between the AFM and FiM spins at the interface. As such, considering a positive cooling field, the spins at the interface are sketched in figure 2.15 a). As the applied field is swept, the FiM moments would prefer to rotate in order to minimize the Zeeman energy, but for a large AFM anisotropy, the AFM moments remain unchanged, thereby generating a unidirectional anisotropy by the interfacial pining of the FiM moments, requiring a stronger field to reverse the magnetization direction (figure 2.15 b)). For a large enough magnetic field (absolute value), this effect is overcome and the spins' orientations are given in figure 2.15 c). However, reversing the field to the direction of the initial cooling field, the FiM moments will switch earlier since the interfacial AFM moments now exert a torque in the direction of the cooling field. Therefore, the result is a shifted hysteresis loop along the field axis.

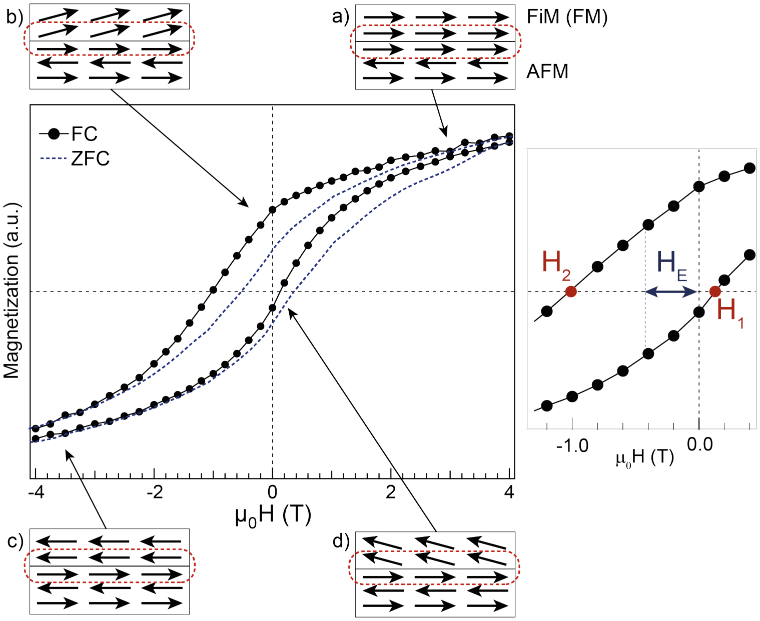

Figure 2.15: The hysteretic shift recorded for the 40 nm bimagnetic Cr substituted Fe-oxide NPs with a representation of the interface between the two magnetic phases for different applied fiels (for the FiM material, the arrows represent the total magnetization). The inset on the right is a zoomed-in version of the hysteresis, illustrating the exchange field.

The exchange field H_E is defined as half the difference between the two recorded fields at magnetization reversal (i.e. the field at which the magnetization is null in each branch of the hysteresis loop - see figure 2.15):

$$H_E = \frac{|H_2| - |H_1|}{2} \tag{2.13}$$

and it provides a measure of the exchange bias. The magnitude of the exchange field thus depends on the anisotropy of the AFM phase and the interfacial area between the two magnetic phases. As it relies on the pinning effect created by the AFM phase, the exchange field vanishes around the Néel temperature of the AFM. However, for SPM systems with a blocking temperature below T_N, the exchange field is often null at temperatures much smaller than T_N. Although the most common indication of the presence of EB is the shifted hysteresis loop, other effects may emerge in the presence of EB, namely increased coercivity[45,46] and temperature and cooling field dependence of the exchange field. The noted coercivity increase is accounted for by the fact that, under the applied magnetic field, if the AFM anisotropy cannot pin the interfacial moments, it will rotate together with the FiM magnetization. In other words, the AFM spins are ”dragged” by the FiM moments, which will translate into a higher energy required, thus resulting in a larger coercivity.

Chapter 3

Experimental techniques

We have seen in Chapter II that the size and shape of NPs can strongly influence their anisotropy and ability to maintain a stable magnetization against the destructive influence of thermal energies. Moreover, the magnetic moments originate from the valence electrons, whose interactions with their surroundings can lead to magnetic ordering. To fully describe the system's magnetic properties, it is thus essential to determine not only the field and temperature-dependent magnetization but also the size, shape, and crystal structure, as well as the chemical surroundings and valence state of the constituent ions.

This chapter aims at describing the experimental techniques used to characterize the systems presented in this thesis. The size, shape and structure of the NPs was investigated by means of electron microscopy and synchrotron x-ray diffraction. The chemical state and element-specific magnetic properties were determined using synchrotron-based spectroscopy techniques coupled with multiplet simulations, while detailed temperature and field-dependent magnetic studies were performed using magnetometry.

3.1 Electron microscopy

"Seeing is believing" is a proverb adopted into the English language from an idea dating back to Ancient Greek times, and represents our innate desire to witness phenomena with our very eyes. In 1610, Galileo Galilei figured out that by cleverly setting what was essentially a simple system of lenses, one can bring the heavenly bodies closer, meaning he could magnify celestial objects from the so-called Macro Universe and view them in more detail[47]. Similarly, Cornelis Drebbel devised a way to magnify small objects from the Micro Universe by using the compound microscope in 1620[48]. A limiting factor in magnifying small objects is the device's resolving power or resolution. An optical microscope's resolution can be restricted by various factors such as imperfections in lenses or misalignments, but the main theoretical limit arises from diffraction effects. Thus, for conventional optical microscopes using visible light, the best achievable diffraction-limited resolution is roughly 200 nm.

In 1924, de Broglie proposed that each particle can have an associated wavelength given by Plank's constant h and its momentum p[49]:

$$\lambda = \frac{h}{p} \tag{3.1}$$

and so, by accelerating electrons to high enough energies, one could reach associated de Broglie wavelengths comparable to and even smaller than atomic distances. This led to the birth of the electron microscope in 1931 by the physicist Ernst Ruska[50]. Even though the diffraction limit problem was solved, the resolution of an electron microscope is given by technical limitations; however, as shall be described below, it is possible to achieve atomic resolution. This section introduces the reader to the electron microscopy techniques used in this work, namely scanning electron microscopy and transmission electron microscopy.

3.1.1 Scanning Electron Microscopy

The scanning electron microscope (SEM) is a versatile tool for studying the morphology of microstructures. It consists of a focused electron beam that is used to scan the surface of interest, and can produce images with nanometer resolution. However, to understand how the signal is generated, we must firstly investigate the interactions between electrons and matter. The two main interactions can be classified as elastic and inelastic processes. The former occurs when the incident electrons are scattered by atomic nuclei and electrons of similar energies, with virtually no energy loss, but a wide-angle directional change. Should the deflection angle be 90° or more, the resulting electrons are called back-scattered electrons and can represent one of the image acquisition signals. On the other hand, inelastic scattering results from interactions with substantial energy transfer between the incident electron beam and the atoms from the sample. The resulting signal can be generated through the emission of specimen electrons after ionization, and they are labelled as secondary electrons. Conventionally, the energies associated are less than 50 eV (typically around $3-5$ eV[51]), so they can only escape from a shallow region below the surface and thus provide the user with the possibility of only studying the surface.

As stated in the introduction of section 3.1, the resolution of the SEM is not restricted by the diffraction limit. Instead, it is given by the size of the focused electron beam and the size of the interaction volume of the sample. Although both can be small, they are larger than atomic distances and so the SEM is not able to image individual atoms, as is a transmission electron microscope (section 3.1.2). However, the SEM is advantageous for imaging comparatively larger sample areas and it is not limited to thin samples as transmission-based techniques. We have used the SEM to image our nanoparticles (**papers III-V**) and determined the general appearance, the surface coverage of the samples and the size distribution. Moreover, SEM was also used for imaging the self-assembled NC in **paper VI** (see figure 3.1 (a)).

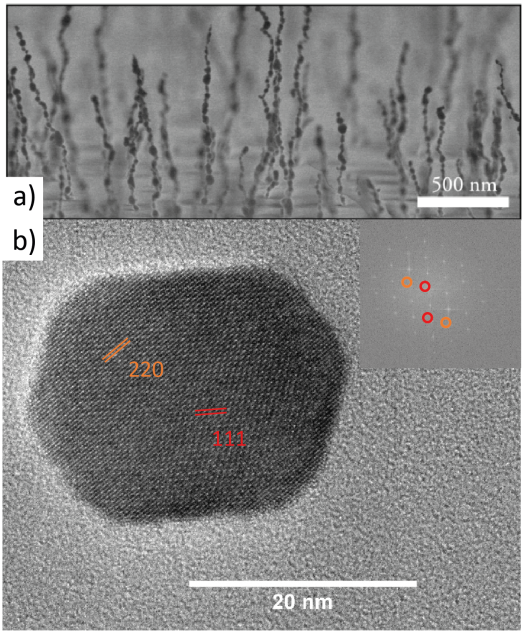

Figure 3.1: a) An SEM image of magnetic self-assembled NCs; b) TEM image of a magnetic NP where "rows" and "lines" of atoms are noticeable; the (111) and (220) lattice planes of the crystal structure are indicated; inset: Fourier transform of the image.

3.1.2 Transmission Electron Microscopy

In a transmission electron microscope (TEM), as the name suggests, the electrons are transmitted through the sample, which entails the requirement of very thin samples, typically of the order of 100 nm or less. Compared to the SEM, the electrons here have higher energies to be able to penetrate through the sample. However, the resolution of an aberration-corrected TEM is of the order of 0.5 Å[52]. The concept of the TEM was demonstrated by Ernst Ruska in 1931, for which he was awarded the

Nobel prize in 1986[53]. The contrast of a TEM may vary with the density or thickness within the sample, in which case it is called mass-thickness contrast. It can also arise as a function of the specific atomic number, crystal structure and orientation, phase shifts and energy losses that electrons experience when they are transmitted through the sample. Using phase contrast, one may observe rows or columns of atoms corresponding to crystallographic planes. Figure 3.1 (b) depicts a TEM image of a Cr substituted Fe_3O_4 NP, which appears single-crystalline with clear lattice fringes corresponding to the atomic rows and columns. As such, it is possible to determine the distances between the atomic planes, and by comparing with known Fe oxides structures, we have identified a spinel structure. However, the TEM image in figure 3.1 represents a 2D projection of the NP, and so more complicated structures become increasingly difficult to identify. As we shall see in section 3.2.3, the NPs also contain small rock salt crystallites which were found by using x-ray diffraction.

Conventionally, the electron beam in a TEM is focused on a small spot on the sample. However, the microscope can also be utilized in scanning mode (STEM) where the mass thickness contrast is enhanced and diffraction contrast is lowered. By detecting the emitted characteristic x-rays from the excited atoms in the sample, elemental information can be gathered and the technique is described in section 3.2.9.

3.1.3 Energy Dispersive X-ray Spectroscopy

Energy dispersive x-ray spectroscopy (EDXS) is a powerful tool for investigating the elemental composition and elemental mapping of small samples when paired with an electron microscope. As the electron beam is focused onto small areas of the sample, the high energy electrons may interact with the atomic species by exciting core-electrons within the atoms. Consequently, a core-hole is created which will cause another electron from a higher energy state to fill it, and thus emitting an x-ray photon in the process. The energy of the released photon is characteristic to the originating atomic species, and so elemental mapping is achieved (please see figure 3.2 for a Cr substituted Fe spinel-oxide nanoparticle).

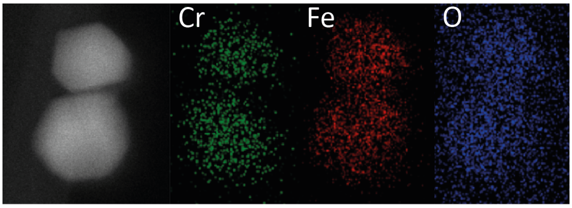

Figure 3.2: EDXS of two Fe-Cr oxide nanoparticles; One can note the homogeneous distribution of both Fe and Cr throughout the particles, as well as their fully oxidized state.

3.2 X-ray based techniques

X-rays were discovered in 1895 by physicist Wilhelm Conrad Röntgen[54] whilst working with so-called Lenard and Crooks tubes. He identified the presence of an unknown type of new radiation, hence the name ”x”, capable of passing through various objects in his lab, such as books, cardboard and papers on his desk. Classically, x-rays are electromagnetic waves with the electric and magnetic fields oscillating in orthogonal planes with respect to each other and the propagation direction, at a wavelength of the order of one Ångström (10^{-10} m). As with any electromagnetic wave, diffraction phenomena are associated with x-rays. However, x-rays can also be absorbed by atoms in certain conditions, in which case it is more convenient to describe them as discrete energy packets called photons. The energy of the photon is related to the wavelength λ by $E = hc/\lambda$, where h is Planck's constant and c is the speed of light in a vacuum.

3.2.1 Light-matter interaction

The interaction between a photon and an electron occurs in two main ways, namely scattering or absorption, as can be seen in figure 3.3. As such, two main experimental techniques, diffraction and spectroscopy, emerge depending on the interaction mechanism and they shall be treated in the following.

In the classical view, an electromagnetic wave's oscillating electric field vector can exert a force on the charge of the electron, causing it to emit an electromagnetic wave since it is accelerated. The scattering process can be elastic, in which case the scattered wave's energy coincides with the incident one, or inelastic, where energy is transferred to the electron in a process known as the Compton effect. However, the elastic scattering is the effect most often utilized in determining the materials' structure. An atom consists of two types of energy levels, specifically core and valence levels. Core levels are tightly bound and localized to the atom's nucleus, whereas valence levels are loosely bound and participate in bonds with neighboring atoms. An x-ray wave can interact and scatter from the localized core electrons and, in a periodic atomic structure, the scattered x-rays may interfere with each other and produce a diffraction pattern that contains information about the geometric arrangement of the atoms or ions. This effect is utilized in x-ray diffraction and the technique is described in section 3.2.3.

The spectroscopic techniques described in this work are fundamentally based on the absorption process and they aim to probe the quantized atomic energy levels and thus provide elemental, chemical and magnetic information. When an x-ray photon's energy matches the energy difference between a valence and core level, a core electron may be promoted to an empty valence state by absorbing the photon's energy, such

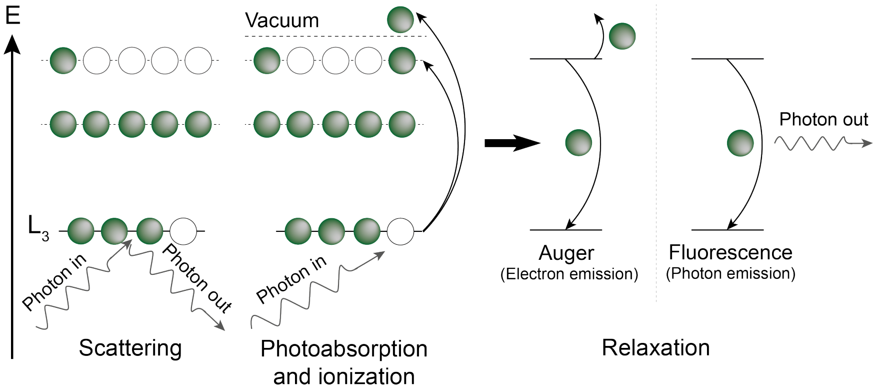
E
Vacuum
L_3
Photon in
Photon out
Photon in
Scattering
Photoabsorption and ionization
Auger
(Electron emission)
Fluorescence
(Photon emission)
Photon out
Relaxation

Figure 3.3: A schematic representation of the scattering and absorption processes (left) and the relaxation pathways that follow (right). Note that in the photoabsorption case the electron is promoted to a higher energy level, whereas in the photoionization case, the electron is ejected into the vacuum.

as depicted in figure 3.3. This is the process behind x-ray absorption spectroscopy and it is described in more detail in section 3.2.5. If the x-ray photon's energy is larger than the binding energy of the electron, it may escape from the sample and the process is known as photoionization (see figure 3.3). The escaped electron, so-called photoelectron, contains chemical and elemental information stemming from its initial core level. This technique is called x-ray photoelectron spectroscopy and it is described in more detail in section 3.2.4.

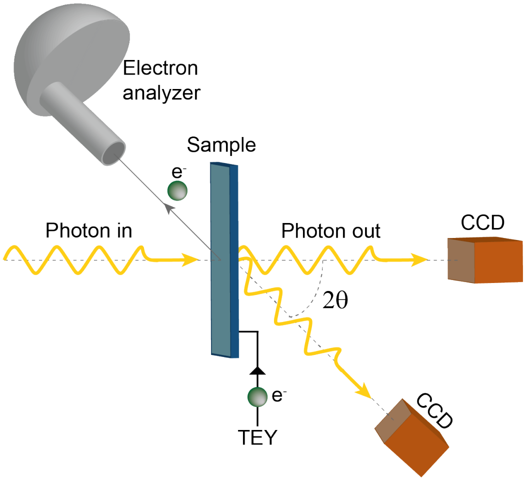
Electron analyzer
Sample
e^-
Photon in
Photon out
CCD
2θ
e^-
TEY
CCD

Figure 3.4: The different detection mechanisms in x-ray experiments employed in this thesis. The photon reaches the sample and can promote an electron into the continuum where it is recorded by an electron analyzer. Moreover, the ejected electrons can create a current at the sample which is then recorded in a scheme called total electron yield (TEY). The transmitted or scattered photons can be detected by a CCD camera either directly or deflected at an angle (2θ).

Both these processes leave behind a core hole that will subsequently be filled by an electron from a higher energy state. This is known as relaxation and the excess energy is taken care of either by the emission of a photon (fluorescence), or by emitting another electron (Auger decay). Both relaxation pathways carry elemental information based on the energy of the emitted photons or Auger electrons and are sketched in figure 3.3. As can be seen in figure 3.4, photons are collected by CCD sensors. For diffraction experiments, the CCD sensors can move at precise angles with respect to the direction of the beam in order to find the constructive interference directions. Furthermore, generated electrons can be collected by an electron analyzer, where the kinetic energies of electrons are measured (photoelectron spectroscopy), or they can induce a current at the sample which is compensated by a drain current flowing from the ground to the sample. The drain current is measured as the total electron yield (absorption spectroscopy).

3.2.2 Synchrotron radiation

To study the interactions between x-rays and matter described in the previous section, an x-ray source with tunable energy and a high photon flux is often required. Conventionally, x-rays are produced from the so-called x-ray tubes where a heavy metal target is bombarded by high-energy electrons. Here, x-rays are emitted by two mechanisms, namely fluorescence (see section 3.1.3 and figure 3.3), and *Bremsstrahlung*, as electrons are scattered by the nuclei in the target. However, x-ray tubes are very inefficient, converting most of the used electricity into heat, resulting in a relatively low photon flux. An alternative x-ray source comes from the field of particle accelerators.

As we have seen in the previous section, an accelerated electron charge emits a photon; it does so even if it is accelerated in a radial trajectory i.e. when the acceleration vector is perpendicular to the velocity. The electrons are accelerated to velocities close to the speed of light and, since they are relativistic, the light is emitted in a cone and it is called synchrotron radiation. It was firstly theorized by Ivanenko and Pomeranchuk[55], but later observed in 1947 at the General Electric synchrotron accelerator by a technician who mistook it for an electric arc discharge. Synchrotron radiation was classified as parasitic at first, since the particle accelerators were designed for nuclear physics experiments. However, due to its noted promising characteristics, nowadays there are dedicated sources purposefully build for the generation of synchrotron x-ray radiation.

A synchrotron storage ring is composed of bending magnets, designed to maintain the electrons in a closed orbit, and straight sections. The radiation is produced either in bending magnets (see figure 3.5) or in insertion devices such as undulators and wigglers (see figure 3.5), which are arrays of permanent magnets arranged in an alternating

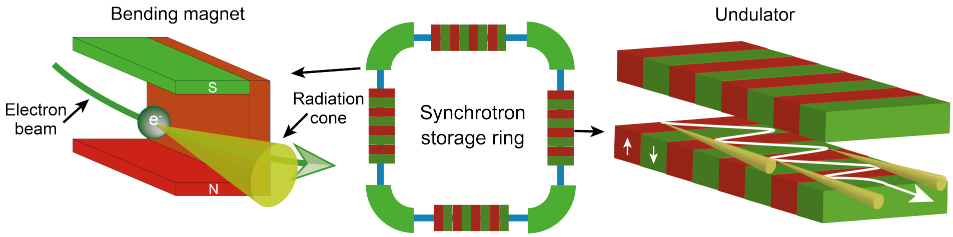

Figure 3.5: A schematic illustration of a synchrotron storage ring (middle) which is made-up of bending magnets (used to steer the electrons in an enclosed loop) and straight sections with insertion devices (undulators and wigglers). Please note that the radiation cone produced by the bending magnet $\theta = 1/\gamma$ has a larger solid angle compared to that of the undulator $\theta = 1/\gamma\sqrt{N}$, where N is the number of undulator periods [56].

fashion placed in the straight sections of the storage ring. The magnetic forces in such devices will cause the electrons to move in an oscillating trajectory and thus emit linearly polarized radiation. The figure of merit for a synchrotron beam is called brilliance and it is a combination of photon flux, the size and spread of the beam and the energy bandwidth (BW) [56]:

$$\text{Brilliance} = \frac{\text{Photons/second}}{(\text{spread mrad})^2(\text{area mm})^2(0.1\%\ \text{BW})} \tag{3.2}$$

and it is approximately 10 orders of magnitude higher than a conventional laboratory x-ray source. Moreover, by adjusting the gap of the insertion device and thereby the magnetic field strength upon the electron beam, a high photon energy tunability is achieved which is a compelling advantage compared to conventional x-ray sources. Depending on the element and the specific core to valence transition, the absorption processes occur at different energies and so photon energy tunability is required for such experiments. Moreover, the magnetic arrays of an undulator insertion device may be shifted with respect to each other such that the produced magnetic forces would constrain a helical trajectory on the electron beam, yielding the generation of circularly polarized light. This enables the study of spin-dependent absorption processes which can provide element-specific magnetic information (sections 3.2.5 and 3.2.6).

The conventional beam-size is ranged between microns and millimeters and thus it is used to gather ensemble averaged information of nano-scale systems. However, the x-ray beam may also be focused e.g. by using Fresnel zone plates and so local ”nanometer” information may be gathered, such as scanning transmission x-ray microscopy (section 3.2.7 and **paper VI**). As can be seen from equation 3.2, a high brilliance entails a high photon flux, which proves to be essential for diluted systems (x-ray magnetic circular dichroism on sub-monolayers of single molecular magnets in

papers I and **II** and x-ray diffraction on NPs in **paper IV**). Furthermore, when using a Fresnel zone plate to focus the x-ray beam, the photon flux reaching the sample is significantly reduced and so a high initial flux is required. The synchrotron radiation based measurements in this thesis were performed at MAX IV, the Advanced Photon Source (APS) and the Swiss Light Source (SLS).

3.2.3 X-ray Diffraction

We have seen that TEM can be used to image single NPs and resolve atomic rows and columns corresponding to parallel planes within the crystal structure. Depending on the system, these so-called lattice planes have specific inter-plane distances d which can be used to distinguish between different crystal structures. However, as the TEM image provides a 2D projection of the 3D crystal, it can be difficult to detect small regions having a slightly different atomic arrangement.

An alternative technique for probing the crystal structure is x-ray diffraction (XRD) and it is based on the interference between x-rays scattered by the core-electrons. In a crystal, the scattered waves interfere constructively along specific directions and thus provide information about the geometric arrangement of the atoms in the structure. As such, XRD provided ensemble-averaged information from all NPs illuminated by the x-rays.

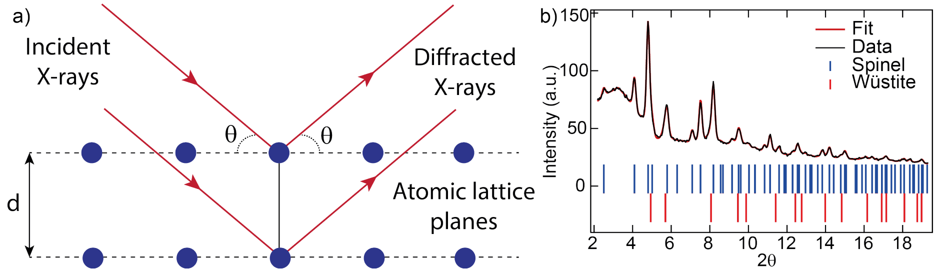

Figure 3.6: a) a schematic of Bragg's law where an incident x-ray beam onto two atomic lattice planes separated by distance d is diffracted under the same angle θ; b) x-ray diffraction pattern recorded for the Cr substituted Fe-spinel oxide nanoparticles in **paper IV**. The fit and the data are given as well as the 2θ positions for each structure used in the fit.

XRD from a crystalline material can be described using Bragg's law, where monochromatic x-rays are specularly reflected ($\theta_i = \theta_f$) in parallel lattice planes separated by distances $d \approx 1$ Å[57]. As such, one does not consider the arrangement of the atoms directly, but the spacing between the lattice planes. The path difference of the x-rays between two adjacent planes is $2d\sin(\theta)$ and constructive interference occurs when it is equal to an integer n times the wavelength λ. The relation describing the condition for constructive interference is known as Bragg's law:

$$n\lambda = 2d\sin\theta \tag{3.3}$$

Therefore, monochromatic x-rays will only interfere constructively along specific directions given by θ in equation 3.3.

Figure 3.6 b) shows the synchrotron recorded XRD pattern for the Cr substituted Fe-spinel oxide NPs in **paper IV**. As can be noted, the fit was achieved by using two structures, namely *spinel* and *wüstite*, illustrated in figure 3.7 a) and b). Both structures share the same face centered cubic (FCC) oxygen lattice with octahedral (B) and tetrahedral (A) interstitial sites. However, the interstitial sites have different cation occupancy among the two structures, thus some lattice planes are the same for both structures and some are different, leading to distinct diffraction peaks. In the bottom part of figure 3.6 b), the 2θ Bragg peaks for the two structures are indicated; all spinel and the unique wüstite diffraction peaks are given. In section 3.1.2 we used FFT analysis on TEM images to obtain structural information. However, the TEM image is a 2D projection of the 3D sample, and so the wüstite subdomains within the host spinel structure cannot be detected with TEM, hence XRD offered crucial information for **paper IV**. The XRD measurements were performed at the 11-ID-B beamline at the Advanced Photon Source, Argonne National Laboratory[58].

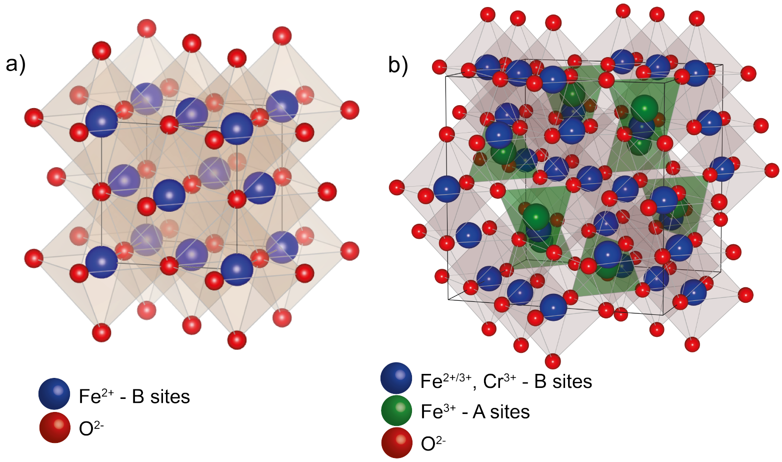

Figure 3.7: Schematic representations of a) wüstite and b) magnetite structures. The atoms in the structure are color coded as: red - oxygen; green and blue - different metallic cations occupying the A and B sites, respectively.

3.2.4 X-ray Photoelectron Spectroscopy

As we saw in Chapter II, the magnetic properties of an ion depend on the occupied valence states and whether the system is e.g. an oxide or a metal. The chemical state and environment of the atoms can be determined using x-ray photoelectron spectroscopy (XPS) where the atomic energy levels of the core-electrons are determined. XPS is based on the photoelectric effect which was discovered in 1887 by Hertz and later described by Albert Einstein for which he was awarded the Nobel prize in 1921[59]. When an electron absorbs an incoming photon, the energy of the photon $E = hc/\lambda$ is transferred to the electron. If the transferred energy is larger than the binding energy of the electron, the so-called photoelectron can escape the surface with a kinetic energy:

$$E_k = \frac{hc}{\lambda} - E_B \tag{3.4}$$

where E_k is the kinetic energy of the electron and E_B the binding energy.

Atomic energy levels are formed due to electrostatic interactions between nuclei and electrons. The core electrons do not participate in the bonding and are still localized to the ions. However, they are affected by changes in the electrostatic potential due to the formation of chemical bonds (different chemical surroundings). This is registered as a shift in the energy of the core levels. Therefore, measuring the core-level shifts provides information of the chemical state of the atom from which the photoelectron was ejected. In an XPS experiment, the core levels are probed by irradiating the sample with monochromatic x-ray light of known energy and thus promoting electrons from their bound core states into the vacuum. The photoelectrons are detected as a function of their kinetic energies using an electron energy analyzer. As such, the binding energy can be determined:

$$E_B = \frac{hc}{\lambda} - E_k$$

An XPS spectrum consists of the number of recorded photoelectrons as a function of binding energy, as shown in figure 3.8. Because of the short mean free path of electrons, XPS experiments are typically carried under ultra-high vacuum conditions and only photoelectrons originating from the top-most atomic layers can escape the sample surface without losing energy, making XPS a surface sensitive technique. However, the probing depth depends on the photoelectrons' kinetic energies; therefore, by increasing the incoming photon energy one can probe deeper into the sample (see equation 3.4).

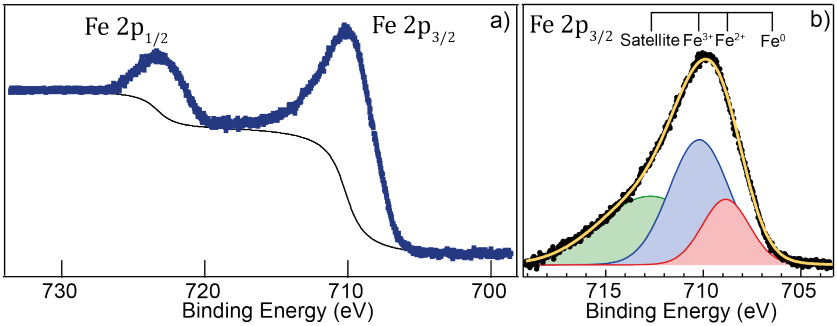

Figure 3.8: XPS spectra of a) Fe $2p$ with the fitted background function and b) Fe $2p_{3/2}$ with the fitted peaks denoting the presence of both di- and tri-valent Fe cations.

XPS was used in **paper IV** to investigate the chemical state of the ions in the Cr substituted Fe-oxide NPs and the Fe $2p_{3/2}$ spectrum is given in figure 3.8 b) after the background subtraction and peak fitting analysis. As can be noted, the analysis revealed the presence of both Fe^{2+} and Fe^{3+} cations whilst no metallic Fe was found. In the divalent and trivalent Fe ions, electron charge is transferred from Fe to O which in turn creates an excess of positive charge onto the ions themselves. As such, more energy is required to remove an electron from an oxide than from the metal and this explains the observed core level shifts in figure 3.8 b): $E_B(\text{Fe}^0) < E_B(\text{Fe}^{2+}) < E_B(\text{Fe}^{3+})$. Moreover, as the photoelectrons "travel" towards the vacuum level, they may interact with the valence electrons and lose kinetic energy, so their binding energies will appear to be higher. This is known as a shake-up satellite structure and it is the green fitted peak in figure 3.8 b). The XPS measurements were performed at the SPECIES beamline[60], MAX IV Laboratory, Lund, Sweden.

3.2.5 X-ray Absorption

X-ray absorption spectroscopy (XAS) is a versatile technique used to study the local electronic structure of atoms by exciting core electrons to higher unoccupied states. Depending on the excited core electron's principal quantum number $n = 1, 2, 3...$, the so-called absorption edges *K, L, M...* are defined. As opposed to photoemission spectroscopies, XAS consits of exciting a core electron to an empty state by tuning the photon energy to match the difference between the two states. Therefore, XAS experiments are performed at synchrotron radiation facilities where photon energy tunability is possible.

The XAS measurements used in **papers I-II, IV** and **VI** were carried out using circularly polarized x-rays. The electric field vector of a circularly polarized wave rotates perpendicular to the propagation direction and, hence, two types can be distinguished, namely right circular polarization (RCP), where the electric field vector rotates clockwise along the propagation direction, and left circular polarization (LCP), where the field vector rotation is counterclockwise. The RCP (LCP) photons carry angular momenta whose projections along the propagation direction are $q = +\hbar$ ($-\hbar$), as opposed to linearly polarized photons where $q = 0$. The transition probability from the initial to the final state is governed by the selection rules which consider the change in quantum numbers of the two states. In the dipole approximation, the interaction between the electric dipole moment operator and the x-ray's electric field is considered, and since the photon carries orbital momentum:

$$\Delta l = \pm 1$$

meaning that e.g. $s \rightarrow s$ transitions are not allowed ($\Delta l \neq 0$). Furthermore, the photon is annihilated in the absorption process, and so the orbital momentum q value is transferred to the sample:

$$\Delta m_l = \pm q$$

Moreover, the spin quantum number is conserved:

$$\Delta s = 0$$

so electrons with a certain initial spin configuration will retain it in the final state.

3.2.6 X-ray Magnetic Circular Dichroism

As described in Chapter II, the atomic magnetic moments of the transition metal and lanthanide ions are given by the $3d$ and $4f$ valence electrons. Given the dipole-selection rules, the magnetic valence states can be probed by resonantly exciting $2p \rightarrow 3d$ and $3d \rightarrow 4f$ transitions, referred to as the $L_{2,3}$ and $M_{4,5}$ absorption edges. Using circularly polarized x-rays, not only the unoccupied levels, but also the spin and orbital moments of the valence state are probed, and the technique utilized is called x-ray magnetic circular dichroism (XMCD). The most facile way to describe the underlying phenomena behind this technique is under the approximation of one electron and a two-step model[61,62]. As we have seen previously, the absorbed photon transfers angular momentum to the electron. If said electron originates from a spin-orbit split level ($2p_{3/2}$ or $2p_{1/2}$), the photon angular momentum will be transferred to the total angular momentum $j = l \pm s$ and so part of it will transfer to the electron spin. As an example, at the L_2 edge ($2p_{1/2} \rightarrow 3d$), whose total angular momentum is $l - s$, RCP light will excite 25% spin-up electrons and 75% spin-down. At the L_3 edge ($2p_{3/2} \rightarrow 3d$), RCP photons will excite 62.5% spin-up electrons and 37.5% spin-down. As can be noted, the ratio between spin-up and spin-down changes at the L_3 edge since the total angular momentum is now $l + s$. A visual example is provided in figure 3.9 for the $L_{2,3}$ edges.

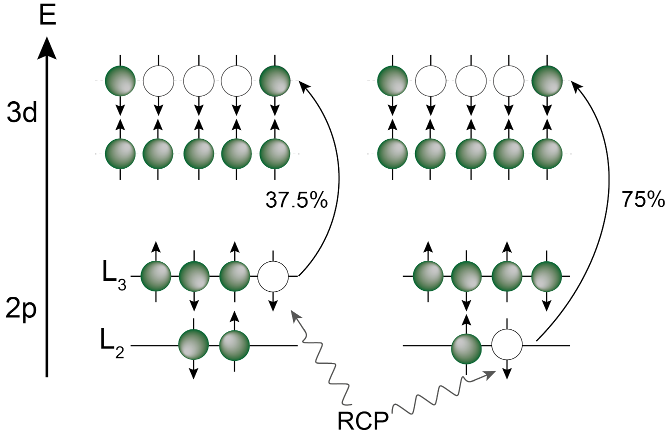

Figure 3.9: The spin-dependent photoabsorption process at the L edge. As can be noted, RCP polarization promotes spin-down electrons for a proportion of 75% at the L_2 edge, and 37.5% at the L_3 edge. Naturally, the remaining percentages represent spin-up electrons for each edge.

The second step relates to the final state. There will be no difference in absorption between RCP and LCP light for a non-magnetic valence state with an equal number of available spin-up and spin-down states. However, if a net magnetic moment is present, there will be a difference in empty states with spin-up and spin-down configurations. As spin is conserved during the transition, empty spin-up states will solely be populated by spin-up electrons and vice-versa, thus converting the exchange-split valence shell into a "spin detector". The absorption intensity will then depend on the number of available final states, making the absorption process spin sensitive.

To obtain the XMCD spectrum, one has to compute the difference in absorption of the two polarizations and plot it as a function of photon energy, such as shown in figure 3.10. By tuning the photon energy to a specific absorption edge, one probes the valence states of a specific element and hence, element specific magnetic information is attained. Moreover, for systems containing multiple magnetic ions, XMCD allows to discriminate between the different magnetic contributions of the different ions. As such, XMCD is essential for studying sub-monolayers of SMMs on surfaces (**papers I and II**), whose signal would be impossible to detect with conventional magnetometry techniques as it would be buried under the substrate's signal originating from a significantly larger volume. As the XMCD signal is proportional to the magnetization projection onto the direction of the x-ray beam, it allows for determining the orientations of the molecular magnetic moments with respect to the substrates' surfaces (**papers I, II**), since it scales as a function of the angle between the direction of magnetization and photon direction. For an isotropic orientation of the endohedral clusters, the orientation of the magnetic easy axes is random and hence there would be no angle-dependent XMCD signal. However, the $Dy_2ScN@C_{80}$ SMM deposited on a surface of Ag(100) has a parallel orientation of the magnetic moments with respect to the surface. In this case, angle-dependent XMCD revealed larger contributions for grazing-incidence angles, thus concluding that the Dy^{3+} ion, and hence the endohedral cluster are oriented almost parallel to the surface, since the magnetic easy axes are oriented along the Dy-N bonds. As such, the XMCD signal can also provide indirect structural information.

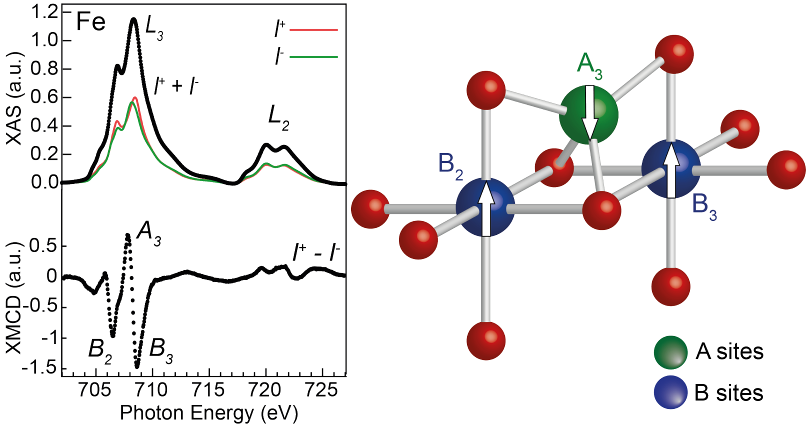

Figure 3.10: Left: XAS and XMCD spectra of the Cr substituted Fe-spinel oxide NPs recorded at the Fe edge under a 6.8 T applied field at the system's base temperature (≈ 2 K). The two RCP and LCP recorded spectra are marked by I^+ and I^- and their sum representing the total XAS signal (shown in the top panel). The main XMCD peaks are labeled corresponding to their interstitial sites and valence; right: a schematic of the magnetic coupling of the spinel-oxide A and B sites. The arrows indicate the average magnetization direction.

Apart from the element specificity, the XMCD signal also offers site-specific magnetic information. Figure 3.10 shows the XAS and XMCD spectra from the Cr substituted Fe-spinel oxide NPs investigated in **paper IV**, allowing to determine the average exchange coupling in the (Fe,Cr)-spinel oxide structure. As such, the three main peaks observed in the Fe-edge XMCD spectrum in figure 3.10 may be attributed to the octahedrally and tetrahedrally coordinated Fe cations: Fe^{2+}_{Oh} and Fe^{3+}_{Oh} in the B sites (peaks B_2 and B_3) and Fe^{3+}_{Td} in the A sites (peak A_3) of the spinel structure. As can be noted, the B sites are ferromagnetically coupled with each other and antiferromagnetically coupled to the ions in the A sites, so a schematic of the average magnetic couplings amongst the spinel-oxide sites may be constructed, such as depicted in the right panel of figure 3.10. Furthermore, the XMCD spectra contain information about the spin and orbital moments separately, based on the spin-orbit splittings ($l \pm s$). One can extract numerical values for the spin and orbital moments using the so-called sum rules (**paper I**)[63,64]. The XAS/XMCD data was measured at the X-treme beamline[65] of the Swiss Light Source (SLS).

3.2.7 Simulations

In a mixed valence system such as the Cr-substituted Fe_3O_4 NPs, the different contributions to the XMCD signal, and hence the magnetic response, can be estimated by means of multiplet simulations. Here, the *Charge Transfer Multiplet for X-ray Absorption* (CTM4XAS) software[66], used to simulate the XMCD spectra of the individual transition metal ions, is described. The software is based upon three different theoretical concepts, namely atomic multiplet theory, crystal field theory and charge transfer theory; describing each in detail is beyond the purpose of this work and thus they shall solely be mentioned in the following.

After choosing the desired atomic element and its formal charge (e.g. Fe^{2+}, Fe^{3+}), the user is prompted with the control of atomic parameters that describe the coupling of the $3d$ electrons, the coupling of the core and valence states and the spin-orbit coupling. The crystal field calculations are carried considering the point group symmetry and the cubic crystal field splitting. Finally, the charge transfer takes effect by allowing control over the charge transfer energy Δ, the Hubbard potential and the core hole potential. For a detailed description, the reader is referred to the work of E. Stavitski *et al*[66] and the references therein.

Finally, the user may plot the calculated XMCD spectra as shown in figure 3.11 where the simulated $L_{3,2}$ edge XMCD spectra of both Fe and Cr are given. The XMCD simulations were used in **paper IV** to determine the individual contributions of the three Fe cations residing in the A and B sites of the spinel structure.

3.2.8 Scanning Transmission X-ray Microscopy

XMCD can be used to obtain local magnetic information from nanoscale objects by focusing the x-ray beam down to tens of nanometers. This concept was utilized in **paper VI** to study the magnetic properties of self-assembled NC composed of ~ 50 nm metallic Co particles, imaged using a technique called scanning transmission x-ray microscopy (STXM). The x-ray beam is focused by a Fresnel zone plate onto the sample and the transmitted light is then detected by a charge coupled device (CCD). The Co NC were deposited onto a TEM grid so that they were freely suspended to minimize substrate absorption and thus increase the contrast. The sample was

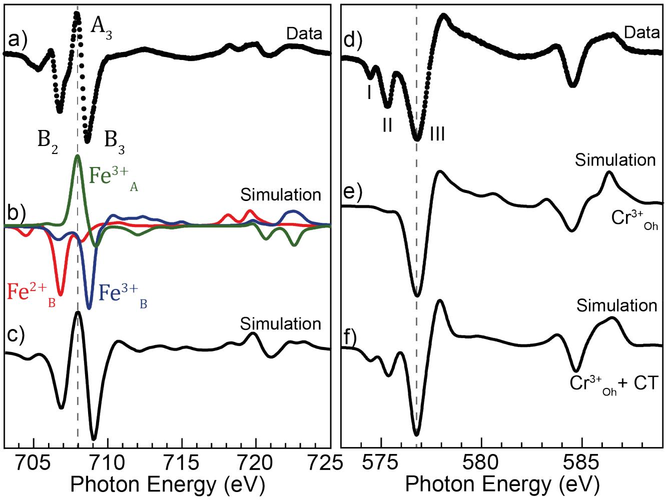

Figure 3.11: a) Fe $L_{3,2}$ edge XMCD data recorded in a 6.8 T magnetic field at 2 K; b) simulated XMCD data for the three Fe cations in the spinel structure; c) weighted sum of the three Fe ions best reproducing the measured data; d) the measured XMCD spectrum at the Cr $L_{3,2}$ edge; e) Cr^{3+} XMCD simulation without charge transfer; f) Cr^{3+} XMCD simulation with charge transfer.

mounted at a 30^o angle with respect to the direction of the incoming photons to be sensitive to the in-plane magnetization. The images were recorded by raster scanning the sample across the focused beam with certain steps in the x and y directions which determine the pixel size. The resolution is then mainly limited by the focal spot of the x-ray beam. This technique requires a synchrotron radiation x-ray beam, where the high brilliance allows for both a small spot and high transmittance.

Figure 3.12 a) and b) shows an SEM and a STXM image from two NCs, one short composed of 4 NPs (NC1) and one much longer with a length of about 2 μm (NC2). Combining SEM and STXM, one is able to gather element specific magnetic information with a resolution approaching that of a single nanoparticle. Comparing the two images, one sees that STXM reproduces the main structural features and resolves the larger NPs along the longer chains. In addition to imaging, XAS can be recorded from a small region by varying the photon energy of the x-ray beam, see figure 3.12 e). Moreover, using circularly polarized x-rays provides magnetic contrast, demonstrating a homogeneous remanent magnetization along $+z$ (bright contrast) for both NCs (figure 3.12 c)). Applying an *in-situ* field of 140 mT along $-z$ results in a magnetization switching (dark contrast) of the shorter chain NC1 and parts of the longer NC2. In the latter case, the change in magnetic contrast indicates domain formation, which was further studied in **paper VI**. The STXM data was recorded at the PolLux beamline[67] of the SLS, Switzerland.

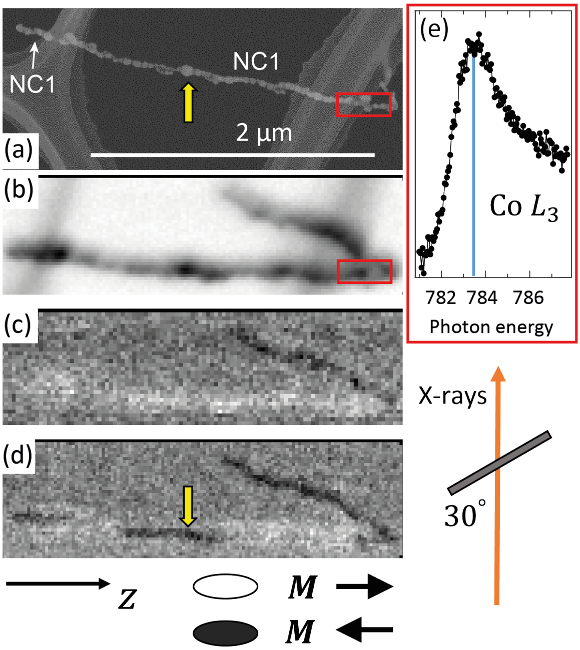

Figure 3.12: a) SEM image of Co NC; STXM images of Co nano-chains: b) the sum of the two circular polarizations - XAS; c) the difference between the two circular polarizations in a +140 mT field - XMCD; d) XMCD under a -140 mT field showing magnetization reversal; e) the XAS spectrum recorded from the red highlighted area. The bright and dark areas indicate the orientation of the magnetization. The sample was oriented at 30° with respect to the photon direction.

3.2.9 X-ray Photoemission Electron Microscopy

X-ray photoemission electron microscopy (XPEEM) is a powerful ”spectromicroscopy” technique based on the spatial distribution of electrons emitted from an x-ray absorption process[68]. Synchrotron radiation is tuned to a certain photon energy and illuminates the sample surface generating photoelectrons. This in turn generates a secondary electron yield which is recorded through an electrostatic and/or electromagnetic lens. Since the x-ray beam can penetrate to depths of tens of nanometers, the photoelectron may originate from an atom relatively deep into the sample surface. However, said photoelectron’s mean free path is of the order of Å, meaning that it will inelastically scatter and thus produce a cascade of secondary electrons with ever decreasing kinetic energies. For low enough kinetic energies (of the order of 1 eV[68]) the electron’s probability to ”escape” the surface is greatly enhanced, thus one is not only sensitive to the surface (as determined by the photoelectron’s mean free path).

XPEEM was used in **paper VI** to image individual Co NPs and an example image is given in figure 3.13. The photon energy is scanned across the absorption edge and the recorded secondary electrons are proportional to the absorption. As such, XAS

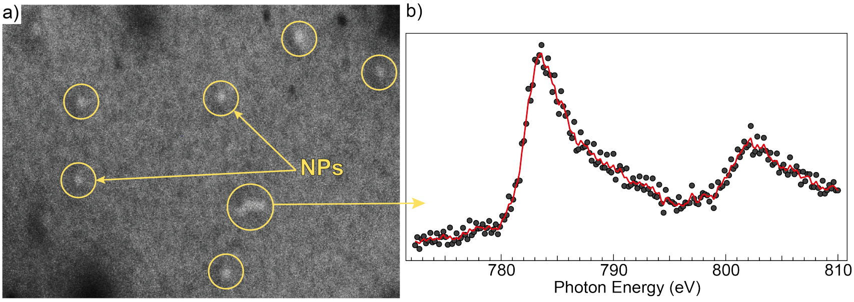

Figure 3.13: a) PEEM image of individual Co nanoparticles (encircled to guide the eye); b) XAS spectrum of a Co particle by recording PEEM images in the shown photon energy range.

spectra of specific regions of interest (in the image) may be constructed, as shown in figure 3.13 b).

3.3 Magnetometry

A large part of the work in this thesis consisted of magnetic characterization of NPs by means of magnetometry. While XMCD is very useful for element and site specific magnetic information, the measurements are performed at synchrotron radiation facilities which entails a relatively limited availability. However, detailed and time-consuming measurements are enabled by using a superconducting quantum interference device (SQUID) magnetometer, which is a highly sensitive device for probing the magnetization from e.g. ensembles of NPs or bulk samples of SMMs. This technique allows for temperature and field dependent measurements, with their precise control.

3.3.1 SQUID

Here the *MPMS3* Vibrating Sample Magnetometer (VSM) with a SQUID by Quantum Design is briefly described. The SQUID was invented in 1964 at the Ford Research Labs[69] and it is a highly sensitive magnetometer capable of detecting a very small magnetic flux, based on the superconducting Josephson effect. The magnetic flux in a loop is defined as $\Phi = \mathbf{B} \cdot \mathbf{S}$, where **B** is the magnetic induction and **S** is the vector area of the loop. However, in a superconductor, the magnetic flux is quantized in units of $\Phi_0 = \mathrm{h}/2\mathrm{e}$, the magnetic flux quantum.

In a so-called Josephson junction (JJ), which consists of two superconductors coupled by a weak link (see figure 3.14), a super-current can flow indefinitely across the junction, even without applying an external voltage. This phenomenon arises from the electrons' behaviour in superconductors, that can form Cooper-pairs resulting from electron-phonon interactions[70]. As such, a Cooper-pair can have a lower energy than the Fermi energy and an integer total spin (0 or 1), making them composite bosons. Because bosons do not obey the Pauli exclusion principle, the majority of Cooper pairs can occupy the same lowest energy state, and can be described by a "macroscopic" wave function (since it directly relates to the super-current that can be measured). As such, it gives rise to a "macroscopic quantum phenomenon". In the absence of a magnetic flux, the super-current I splits into two equal currents I_a and I_b around a ring with two JJs (see figure 3.14). In the presence of a magnetic flux, a screening current I_s is induced and circulates the ring as shown in figure 3.14; when the current in either branch exceeds a critical current of the JJ I_c, a voltage appears across the JJ. As such, in the presence of a magnetic flux, the two currents I_a and I_b exhibit a phase shift determined by the magnitude of the flux. The two will interfere constructively if the flux is an integer of the magnetic flux quantum Φ_0. Both the super-current and the voltage measured across the ring will vary with a period of Φ_0 as[71]:

$$\Delta V = \frac{R}{L}\Delta\Phi \tag{3.5}$$

where L is the self inductance of the SQUID and R is a shunt resistor. As such, the SQUID is an ultra-sensitive magnetic flux to voltage converter.

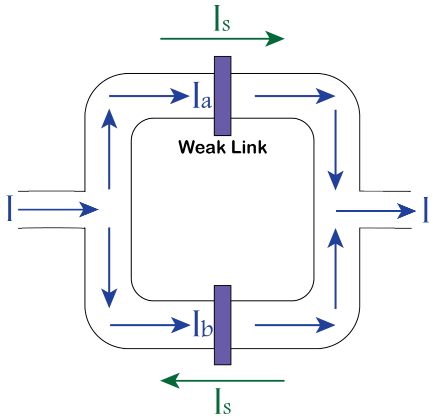

Figure 3.14: A schematic drawing of the DC SQUID composed of two JJs.

A VSM with a SQUID operates by oscillating a magnetic sample vertically with or without an applied magnetic field. The oscillating magnetic field originating from the sample creates a magnetic flux that induces a current in the superconducting pick-up coils, which is subsequently transported to another superconducting coil outside of the measurement chamber, typically in a magnetically shielded chamber. Here, the induced current in the signal coil (see figure 3.15) is used to recreate the magnetic signal from the sample, in the presence of a SQUID. As mentioned previously, the SQUID converts the magnetic signal into a voltage (as in equation 3.5), which is later amplified and conventionally manipulated by a computer.

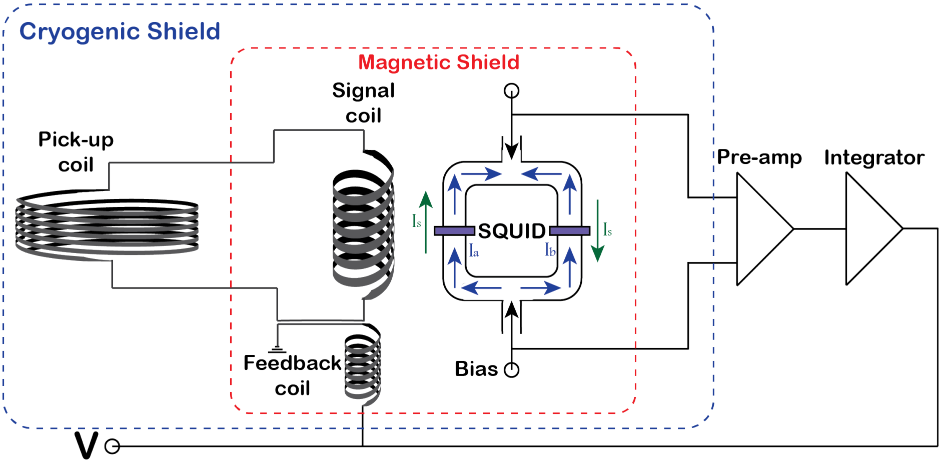
Cryogenic Shield
Magnetic Shield
Signal coil
Pick-up coil
Pre-amp
Integrator
I_s
SQUID
I_a
I_b
I_s
Feedback coil
Bias
V

Figure 3.15: A schematic drawing of the working principle of a SQUID magnetometer.

The sensitivity of the *MPMS3* VSM with a SQUID is of the order of 10^{-11} Am^2, or, as it is conventionally reported for small magnetic moments, 10^{-8} emu[72], where 1 emu (electromagnetic unit) is 10^{-3} Am^2. We have used the SQUID to measure the magnetization of both SMMs and NPs as a function of field and temperature (**papers I-V**).

Chapter 4

Summary of papers

The aim of this thesis is the characterization of magnetic nanoscale systems, namely SMMs, magnetic NPs and NCs. Papers I and II investigate the magnetic properties of SMMs on surfaces. Papers III-V provide the synthesis and characterization of bi-magnetic NPs and the emergence of EB. Paper VI provides an x-ray microscopy study of the magnetization reversal in Co nanochains (NC).

Paper I

This paper reports on the magnetic properties of fullerene SMMs $DySc_2N@C_{80}$ and $Dy_2ScN@C_{80}$ functionalized via $1,3$-dipolar cycloaddiation with surface-anchoring tioether groups. Magnetometry measurements on functionalized and non - functionalized bulk samples reveal that cycloaddition significantly affects magnetic bistability. Interestingly, the blocking temperature increased for $DySc_2N@C_{80}$, while it decreased for $Dy_2ScN@C_{80}$ and substantially reduced the coercivity. Self-assembled monolayers were chemically prepared on Au(111) and studied using XMCD. Both systems exhibit low temperature hysteresis but shorter relaxation times compared to the bulk measurements, attributed to the direct contacts between the fullerenes and the substrates. The fullerenes are mobile at room temperature but freeze in random orientations at lower temperatures, thus exhibiting randomly oriented magnetic moments, as determined from angle-dependent XMCD measurements.

Paper II

In this paper, the magnetic properties of monolayers of $Dy_2ScN@C_{80}$ SMM sublimated onto Au(111), Ag(100) and MgO|Ag(100) surfaces are investigated by means of XMCD and *ab initio* calculations. Firstly, it is found that the angular dependence of the XMCD signal from the Dy^{3+} ions is almost isotropic for the SMMs deposited on Au(111) and the insulating MgO thin film on Ag(100), but highly anisotropic for the Ag(100) surface. As the Dy moments are oriented along the Dy-N bond, the aforementioned angular dependence sheds light onto the orientations of the Dy_2ScN clusters on the surfaces, entailing a random orientation of the cluster on the Au(111) and MgO|Ag(100) and a parallel orientation with respect to the Ag(100) surface. Moreover, element-specific magnetization curves recored using XMCD revealed the presence of hysteresis at 2 K with a coercive field of roughly 0.4 T for all three surfaces, with no apparent dependence on the substrate.

Paper III

This paper describes the generation of mixed-metal FeCr and FeMn NPs using an aerosol technique based on spark ablation. Varying the carrier gas resulted in oxidized and metallic systems, where the latter formed a self-passivating oxide shell when exposed to the atmosphere. Moreover, the transition-metal ratio in the NPs was almost identical to that of the seed electrodes. Magnetization measurements demonstrated the feasibility of studying the magnetic properties of aerosol-generated particles at different coverages, ranging from sparsely placed NPs to larger clusters.

Paper IV

This paper is a characterization study of the structural, chemical and magnetic properties of 40 nm Cr substituted Fe_3O_4 spinel oxide NPs. The structural characterization was accomplished by means of XRD coupled with electron microscopy, and the determined structure was that of a spinel oxide hosting 4 nm rock salt (Fe_xO) subdomains. It was calculated that approximately 80% of the particles are composed of spinel with the remainder 20% Fe_xO. The chemical analysis studied by XPS suggested a mixed valence system with both Fe^{2+} and Fe^{3+} present, indicating an inverse spinel structure similar to magnetite Fe_3O_4. The XMCD data paired with multiplet simulations further supported a Fe_3O_4 structure and revealed that the Cr^{3+} ions occupy the octahedral sites, where they are FM coupled to the Fe ions in the same sub-lattice and AFM coupled to the tetrahedrally coordinated Fe ions. The NPs are thus bimagnetic with a 40 nm FiM spinel structure occupied by 4 nm AFM Fe_xO subdomains. Cooling in a magnetic field across the Néel temperature of the FeO subdomains resulted in an exceptionally large EB, attributed to the large interface area between the two magnetic phases. The unique structure is attributed to the presence of Cr and the formation of FeCr-spinel-oxide that acts as a diffusion barrier, preventing the complete oxidation and transformation of the FeO subdomains into magnetite.

Paper V

This paper is a continuation of paper IV and investigates the influence of the particle size on the formation of the Fe_xO subdomains and the emergence of EB. As such, the magnetic properties of three FeCr systems of sizes 10, 20 and 40 nm are investigated by means of SQUID magnetometry. The field-cooled hysteresis loops reveal the presence of significant EB for the 40 and 20 nm systems, which decreases in magnitude with decreasing the NP diameter. Furthermore, only minor exchange fields are observed for the 10 nm particles. This behavior is attributed to the lower presence of the metastable Fe_xO subdomains due to the higher likelihood of being converted into the more stable $(Fe,Cr)_3O_4$ phase as the particle diameter is reduced.

Paper VI

In this paper the magnetization reversal in Co NC is investigated. The NC were prepared via direct-self assembly of individual Co NPs with diameters of approximately 50 nm and the magnetization was imaged by means of STXM under *in-situ* applied magnetic fields. The analysis shows the strong preference of the magnetization along the chains. Furthermore, an applied field of -140 mT switches the magnetization direction in shorter chains, enabled by smaller shape anisotropy. As longer NC have a larger shape anisotropy, magnetization switching is more difficult. However, the magnetization can switch in the presence of a larger NP within the chain, as it facilitates domain-wall nucleation. The latter is moreover confirmed by micromagnetic simulations. It was concluded that the structures exhibit a large shape anisotropy that forces the magnetization direction to lie along the chain.

Chapter 5

Conclusions and outlook

Monolayers of endofullerene SMMs were deposited and studied on conducting and insulating substrates. The monolayers were formed by UHV sublimation and chemical deposition of endofullerenes functionalized via $1,3$-dipolar cycloaddition with surface-anchoring tioether groups. The cycloaddition method showed improved magnetic response for $DySc_2N@C_{80}$ and worse for $Dy_2ScN@C_{80}$. The different substrates appeared to influence the order of the clusters but did not play a role in the magnetic bistability. As contact between the SMMs and an electrode is necessary for potential spintronic applications, this study not only showed that $Dy_2ScN@C_{80}$ fulfills this criterion, but also offered a detailed description of the magnetic behavior on three different surfaces by means of XMCD angular dependence and sum rules analysis.

Recently, the principal investigators in **papers I** and **II** managed to push the magnetic bistability up to a record high temperature of 28 K for monolayers of $Tb_2@C_{80}(CH_2Ph)$ functionalized with pyrene on graphene and highly oriented pyrolitic graphite[73]. Single-walled carbon nanotubes, which are "rolled up" graphene sheets, can be functionalized with SMMs with a great potential in molecular spintronics[74]. In this regard, endofullerenes have suitable diameters for encapsulation in carbon nanotubes and therefore the generation of 1D arrays of SMMs. For the $Dy_nSc_{3-n}N@C_{80}$ SMM, magnetic hysteresis has been demonstrated for n = 1[75] and partial intramolecular ordering for n = 2[76]. Considering the impressive results from the $Tb_2@C_{80}(CH_2Ph)$ monolayers on graphene, it would be interesting to study 1D arrays of the latter SMM packed into carbon nanotubes.

In **paper III** the NPs synthesis was described, demonstrating the potential of spark ablation for generating mixed-metal magnetic nanoparticles with an elemental composition tuned by the seed electrodes. As such, metallic and oxidized FeCr and FeMn NPs were synthesized by adjusting the carrier gas. The FeMn systems exhibited a Janus structure (see inset in figure 5.1 a)) with a metallic Fe core, a Fe-oxide shell and a Mn-oxide domain. The Fe core is FM and the Fe-oxide shell most likely has a FiM spinel structure. The Mn-oxide domain is presumed to be AFM, which would explain the presence of EB found in a preliminary study after cooling the particles down to 2 K in a 7 T field (see figure 5.1 a)).

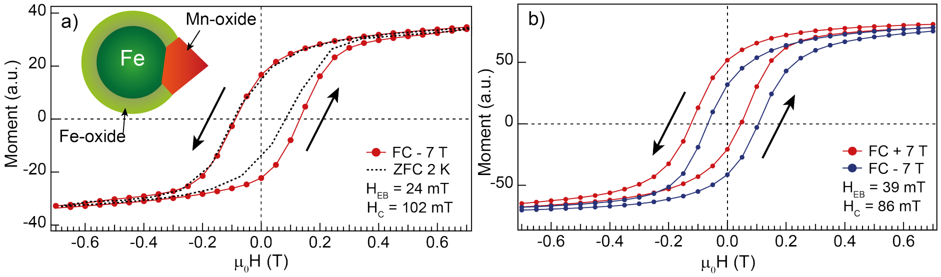

Figure 5.1: a) ZFC and -7 T FC hysteresis loops of the FeMn NP system with a schematic of a Janus particle inset; b) ±7 T FC hysteresis loops for the $Fe_{60}Cr_{40}$ NP system.

The detailed structural and magnetic characterization of the FeCr-oxide 40 nm bimagnetic NPs revealed a novel structure of FiM spinel with embedded AFM subdomains, and the presence of a large EB. The structure was attributed to the presence of Cr which creates a diffusion barrier, preventing the complete conversion from wüstite into magnetite. It would be of particular interest to investigate the field-cooled behavior of the FeCr systems by means of XMCD: field-cooled XMCD signal coupled with simulations to assess the different changes in the contributions of the individual ions and field-cooled XMCD hysteresis loops, for a deeper understanding of the EB mechanism.

The emergence of EB for the FeCr-oxide systems was furthermore investigated as a function of particle size. Both 40 and 20 nm NPs show the presence of EB with decreasing magnitude as the NP's diameter decreases, whereas the 10 nm particles show much smaller EB. Since the inclusion of Cr plays a key role in the AFM subdomains formation, it would also be particularly interesting to make a study based on the Cr concentration. Preliminary results for a NPs system with a Fe : Cr ratio of 60 : 40 are shown in figure 5.1 b). As can be noted, even at a much higher Cr concentration, the presence of EB is identified, however, with a significantly smaller shift as compared to the NPs with a higher concentration of Fe. Moreover, preliminary data of Fe-oxide NPs exhibits almost zero EB, indicating an absence of Fe_xO clusters and thus supporting our hypothesis of Cr playing a key role in the formation of the AFM subdomains.

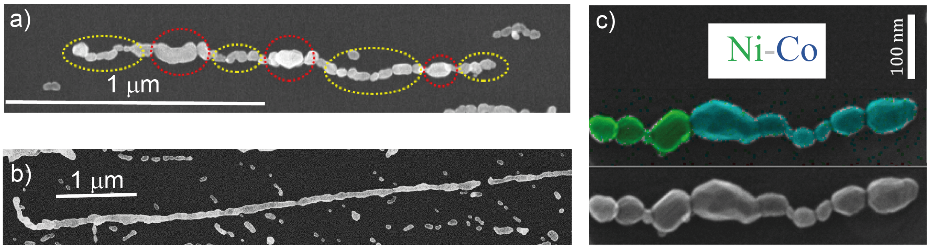

Figure 5.2: SEM images of: a) size-modulated NCs, b) post-annealing induced "fusion" of particles in the NC and c) segmented Ni and Co NCs.

The versatility of the technique provides a wide range of magnetic material systems that could be studied with a nanoscale metal ratio that can be macroscopically tuned by the composition of the electrodes. Furthermore, recent studies have shown that the NPs can be post-processed while still suspended in the inert carrier gas, where core-shell systems were generated by transporting the NPs through a Zn vapor. These results open up new avenues for coating and preventing small metal alloyed NPs from oxidizing, a problem found in many systems. Moreover, instead of Zn, one could evaporate different magnetic materials to form tailored bimagnetic core-shell systems.

The Co nanochains (NC) were also synthesized by means of spark ablation through self-assembling size selected Co NPs under an applied magnetic field, as described in **paper VI**. A large shape anisotropy causes the magnetization to lie along the NCs and small magnetic fields (140 mT) cannot reverse the magnetization, except for shorter chains. However, in the presence of a larger NP within the chain, magnetization reversal and domain formation can occur, due to the larger NP acting as a nucleation center. Since the measurements for **paper VI** were performed, there has been significant progress made in the generation of NCs: i) controlled generation of size-modulated NCs (see figure 5.2 a)), which would offer further insight into the role of the larger particle on the domain formation; ii) post-annealing of the NC, causing the constituent NPs to "fuse" together and thus increasing the interparticle exchange coupling. As such, for high enough temperatures, the NC will transform into nanowires, as seen in figure 5.2 b); iii) segmented NCs (see figure 5.2 c)), which consist of NCs formed by multiple magnetic phases - this would offer the possibility to not only study different magnetically ordered phases and EB, but also hard-soft exchange-coupled permanent magnets, thus offering strategies for next generation rare-earth-free permanent magnets.

References

[1] Mark Re. Tech talk on hdd areal density. Seagate, 2018.

[2] John MD Coey. *Magnetism and magnetic materials*. Cambridge university press, 2010.

[3] W Maver. Electricity, its history and progress. *The Encyclopedia Americana*, 10: 174–6, 1918.

[4] L Pearce Williams. Faraday's discovery of electromagnetic induction. *Contemporary Physics*, 5(1):28–37, 1963.

[5] Narayan Poudyal and J Ping Liu. Advances in nanostructured permanent magnets research. *Journal of Physics D: Applied Physics*, 46(4):043001, 2012.

[6] Oliver Gutfleisch, Matthew A Willard, Ekkes Brück, Christina H Chen, SG Sankar, and J Ping Liu. Magnetic materials and devices for the 21st century: stronger, lighter, and more energy efficient. *Advanced materials*, 23(7): 821–842, 2011.

[7] Robert E Camley and J Barnaś. Theory of giant magnetoresistance effects in magnetic layered structures with antiferromagnetic coupling. *Physical review letters*, 63(6):664, 1989.

[8] Stuart A Wolf and Daryl Treger. Spintronics: A new paradigm for electronics for the new millennium. *IEEE Transactions on Magnetics*, 36(5):2748–2751, 2000.

[9] F Donati, S Rusponi, S Stepanow, C Wckerlin, A Singha, L Persichetti, R Baltic, K Diller, F Patthey, E Fernandes, et al. Magnetic remanence in single atoms. *Science*, 352(6283):318–321, 2016.

[10] FD Natterer, K Yang, W Paul, P Willke, T Choi, and T Greber. Reading and writing single-atom magnets. *Nature*, 543(7644):226–228.

[11] Roberta Sessoli, Dante Gatteschi, Andrea Caneschi, and MA Novak. Magnetic bistability in a metal-ion cluster. *Nature*, 365(6442):141–143, 1993.

[12] Naoto Ishikawa, Miki Sugita, Tadahiko Ishikawa, Shin-ya Koshihara, and Youkoh Kaizu. Lanthanide double-decker complexes functioning as magnets at the single-molecular level. *Journal of the American Chemical Society*, 125(29): 8694–8695, 2003.

[13] Lapo Bogani and Wolfgang Wernsdorfer. Molecular spintronics using single-molecule magnets. In *Nanoscience and technology: a collection of reviews from nature journals*, pages 194–201. World Scientific, 2010.

[14] J Tejada, EM Chudnovsky, E Del Barco, JM Hernandez, and TP Spiller. Magnetic qubits as hardware for quantum computers. *Nanotechnology*, 12(2):181, 2001.

[15] C-H Chen, DS Krylov, SM Avdoshenko, F Liu, L Spree, R Westerström, C Bulbucan, M Studniarek, J Dreiser, AUB Wolter, et al. Magnetic hysteresis in self-assembled monolayers of dy-fullerene single molecule magnets on gold. *Nanoscale*, 10(24):11287–11292, 2018.

[16] Vassil Skumryev, Stoyan Stoyanov, Yong Zhang, George Hadjipanayis, Dominique Givord, and Josep Nogués. Beating the superparamagnetic limit with exchange bias. *nature*, 423(6942):850–853, 2003.

[17] PK Manna and SM Yusuf. Two interface effects: Exchange bias and magnetic proximity. *Physics Reports*, 535(2):61–99, 2014.

[18] Jae-Hyun Lee, Jung-tak Jang, Jin-sil Choi, Seung Ho Moon, Seung-hyun Noh, Ji-wook Kim, Jin-Gyu Kim, Il-Sun Kim, Kook In Park, and Jinwoo Cheon. Exchange-coupled magnetic nanoparticles for efficient heat induction. *Nature nanotechnology*, 6(7):418–422, 2011.

[19] Z Nemati, J Alonso, H Khurshid, MH Phan, and H Srikanth. Core/shell iron/iron oxide nanoparticles: are they promising for magnetic hyperthermia? *RSC advances*, 6(45):38697–38702, 2016.

[20] Aidin Lak, Dina Niculaes, George C Anyfantis, Giovanni Bertoni, Markus J Barthel, Sergio Marras, Marco Cassani, Simone Nitti, Athanassia Athanassiou, Cinzia Giannini, et al. Facile transformation of FeO/Fe_3O_4 core-shell nanocubes to Fe_3O_4 via magnetic stimulation. *Scientific reports*, 6(1):1–12, 2016.

[21] Alberto López-Ortega, Marta Estrader, German Salazar-Alvarez, Alejando G Roca, and Josep Nogués. Applications of exchange coupled bi-magnetic

hard/soft and soft/hard magnetic core/shell nanoparticles. *Physics Reports*, 553: 1–32, 2015.

[22] E Lottini, A López-Ortega, G Bertoni, S Turner, M Meledina, G Van Tendeloo, C de Julián Fernández, and C Sangregorio. Strongly exchange coupled core| shell nanoparticles with high magnetic anisotropy: a strategy toward rare-earth-free permanent magnets. *Chemistry of Materials*, 28(12):4214–4222, 2016.

[23] Maria E Messing, Rasmus Westerström, Bengt O Meuller, Sara Blomberg, Johan Gustafson, Jesper N Andersen, Edvin Lundgren, Richard van Rijn, Olivier Balmes, Hendrik Bluhm, et al. Generation of Pd model catalyst nanoparticles by spark discharge. *The Journal of Physical Chemistry C*, 114(20):9257–9263, 2010.

[24] Jeotikanta Mohapatra, Meiying Xing, Jacob Elkins, Julian Beatty, and J Ping Liu. Extraordinary magnetic hardening in nanowire assemblies: the geometry and proximity effects. *Advanced Functional Materials*, 31(13):2010157, 2021.

[25] Masamitsu Hayashi, Luc Thomas, Charles Rettner, Rai Moriya, Yaroslaw B Bazaliy, and Stuart SP Parkin. Current driven domain wall velocities exceeding the spin angular momentum transfer rate in permalloy nanowires. *Physical review letters*, 98(3):037204, 2007.

[26] Stuart SP Parkin, Masamitsu Hayashi, and Luc Thomas. Magnetic domain-wall racetrack memory. *Science*, 320(5873):190–194, 2008.

[27] Joachim Stöhr and Hans Christoph Siegmann. Magnetism. *Solid-State Sciences. Springer, Berlin, Heidelberg*, 5, 2006.

[28] Nicola A Spaldin. *Magnetic materials: fundamentals and applications*. Cambridge university press, 2010.

[29] HN Russell and FA Saunders. New regularities in the spectra of the alkaline earths. *Atomic Spectra: The Commonwealth and International Library: Selected Readings in Physics*, page 206, 2013.

[30] Friedrich Hund. *Linienspektren: Und Periodisches System der Elemente*, volume 4. Springer-Verlag, 2013.

[31] Alex Hubert and Rudolf Schäfer. *Magnetic domains: the analysis of magnetic microstructures*. Springer Science & Business Media, 2008.

[32] Robert M White, Robert M White, and Bradford Bayne. *Quantum theory of magnetism*, volume 1. Springer, 1983.

[33] KH Jürgen Buschow. *Encyclopedia of materials: science and technology*, volume 1. Elsevier, 2001.

[34] IS Jacobs and FE Luborsky. Magnetic anisotropy and rotational hysteresis in elongated fine-particle magnets. *Journal of Applied Physics*, 28(4):467–473, 1957.

[35] Henri Amar. On the width and energy of domain walls in small multi-domain particles. *Journal of Applied Physics*, 28(6):732–733, 1957.

[36] Alberto P Guimarães and Alberto Passos Guimaraes. *Principles of nanomagnetism*, volume 7. Springer, 2009.

[37] Louis Néel. Influence des fluctuations thermiques sur l'aimantation de grains ferromagnétiques très fins. *Comptes Rendus Hebdomadaires Des Seances De L Academie Des Sciences*, 228(8):664–666, 1949.

[38] Ignacio Javier Bruvera, Pedro Mendoza Zélis, M Pilar Calatayud, Gerardo Fabián Goya, and Francisco Homero Sánchez. Determination of the blocking temperature of magnetic nanoparticles: The good, the bad, and the ugly. *Journal of Applied Physics*, 118(18):184304, 2015.

[39] Harold W Kroto, James R Heath, Sean C O'Brien, Robert F Curl, and Richard E Smalley. C_60: Buckminsterfullerene. *Nature*, 318(6042):162–163, 1985.

[40] S Stevenson, G Rice, T Glass, K Harich, F Cromer, MR Jordan, J Craft, E Hadju, R Bible, MM Olmstead, et al. Small-bandgap endohedral metallofullerenes in high yield and purity. *Nature*, 401(6748):55–57, 1999.

[41] Rasmus Westerström, Jan Dreiser, Cinthia Piamonteze, Matthias Muntwiler, Stephen Weyeneth, Harald Brune, Stefano Rusponi, Frithjof Nolting, Alexey Popov, Shangfeng Yang, et al. An endohedral single-molecule magnet with long relaxation times: $DySc_2N@C_{80}$. *Journal of the American Chemical Society*, 134 (24):9840–9843, 2012.

[42] Rasmus Westerström, Jan Dreiser, Cinthia Piamonteze, Matthias Muntwiler, Stephen Weyeneth, Karl Krämer, Shi-Xia Liu, Silvio Decurtins, Alexey Popov, Shangfeng Yang, et al. Tunneling, remanence, and frustration in dysprosium-based endohedral single-molecule magnets. *Physical Review B*, 89(6):060406, 2014.

[43] Manh-Huong Phan, Javier Alonso, Hafsa Khurshid, Paula Lampen-Kelley, Sayan Chandra, Kristen Stojak Repa, Zohreh Nemati, Raja Das, Óscar Iglesias, and Hariharan Srikanth. Exchange bias effects in iron oxide-based nanoparticle systems. *Nanomaterials*, 6(11):221, 2016.

[44] Surender Kumar Sharma. *Exchange bias: from thin film to nanogranular and bulk systems*. CRC Press, 2017.

[45] William H Meiklejohn and Charles P Bean. New magnetic anisotropy. *Physical review*, 102(5):1413, 1956.

[46] Josep Nogués, J Sort, V Langlais, V Skumryev, S Suriñach, JS Muñoz, and MD Baró. Exchange bias in nanostructures. *Physics reports*, 422(3):65–117, 2005.

[47] David Topper. Giants of delft: Johannes vermeer and the natural philosophers: The parallel search for knowledge during the age of discovery. *Leonardo*, 37(3): 258–259, 2004.

[48] Raymond J Seeger. *Men of Physics: Galileo Galilei, His Life and His Works*. Elsevier, 2016.

[49] Louis de Broglie. *Recherches sur la theorie des quanta.* PhD thesis, Univ. de Paris., 1924.

[50] E Ruska. The development of the electron and of electron microscopy microscope. *Bioscience Reports*, 7, 1987.

[51] Weilie Zhou, Robert Apkarian, Zhong Lin Wang, and David Joy. *Fundamentals of Scanning Electron Microscopy (SEM)*, pages 1–40. Springer New York, New York, NY, 2007.

[52] Rolf Erni, Marta D Rossell, Christian Kisielowski, and Ulrich Dahmen. Atomic-resolution imaging with a sub-50-pm electron probe. *Physical review letters*, 102 (9):096101, 2009.

[53] NobelPrize.org. Nobel Prize Outreach AB 2021, 1986. URL `https://www.nobelprize.org/prizes/physics/1986/summary/`.

[54] Arthur Stanton. Wilhelm conrad röntgen on a new kind of rays: translation of a paper read before the würzburg physical and medical society, 1895. *Nature*, 53 (1369):274–276, 1896.

[55] Herbert C Pollock. The discovery of synchrotron radiation. *American Journal of Physics*, 51(3):278–280, 1983.

[56] Klaus Wille. *The physics of particle accelerators: an introduction*. Clarendon Press, 2000.

[57] Charles Kittel. *Introduction to Solid State Physics*. Wiley, 8 edition, 2004. ISBN 9780471415268.

[58] U Rütt, MA Beno, J Strempfer, G Jennings, C Kurtz, and PA Montano. Diffractometer for high energy X-rays at the APS. *Nuclear Instruments and Methods in Physics Research Section A: Accelerators, Spectrometers, Detectors and Associated Equipment*, 467:1026–1029, 2001.

[59] NobelPrize.org. Nobel Prize Outreach AB 2021, 1921. URL `https://www.nobelprize.org/prizes/physics/1921/einstein/facts/`.

[60] Samuli Urpelainen, Conny Såthe, Walan Grizolli, Marcus Agåker, Ashley R Head, Margit Andersson, S-W Huang, Brian N Jensen, Erik Wallén, Hamed Tarawneh, et al. The SPECIES beamline at the MAX IV Laboratory: a facility for soft X-ray RIXS and APXPS. *Journal of synchrotron radiation*, 24(1):344–353, 2017.

[61] J Stöhr. Exploring the microscopic origin of magnetic anisotropies with X-ray magnetic circular dichroism (XMCD) spectroscopy. *Journal of Magnetism and Magnetic Materials*, 200(1-3):470–497, 1999.

[62] G Schüz, W Wagner, W Wilhelm, et al. Absorption of circularly polarized X-rays in iron [j]. *Phys Rev Lett*, 58(7):737, 1987.

[63] Paolo Carra, BT Thole, Massimo Altarelli, and Xindong Wang. X-ray circular dichroism and local magnetic fields. *Physical Review Letters*, 70(5):694, 1993.

[64] BT Thole, Paolo Carra, F Sette, and Gerrit van der Laan. X-ray circular dichroism as a probe of orbital magnetization. *Physical review letters*, 68(12):1943, 1992.

[65] Cinthia Piamonteze, Uwe Flechsig, Stefano Rusponi, Jan Dreiser, Jakoba Heidler, Marcus Schmidt, Reto Wetter, Marco Calvi, Thomas Schmidt, Helena Pruchova, et al. X-treme beamline at SLS: X-ray magnetic circular and linear dichroism at high field and low temperature. *Journal of synchrotron radiation*, 19 (5):661–674, 2012.

[66] Eli Stavitski and Frank MF De Groot. The CTM4XAS program for EELS and XAS spectral shape analysis of transition metal L edges. *Micron*, 41(7):687–694, 2010.

[67] J Raabe, G Tzvetkov, U Flechsig, M Böge, A Jaggi, B Sarafimov, MGC Vernooij, T Huthwelker, H Ade, D Kilcoyne, et al. PolLux: A new facility for soft x-ray spectromicroscopy at the Swiss Light Source. *Review of scientific instruments*, 79 (11):113704, 2008.

[68] Philip Willmott. *An introduction to synchrotron radiation: techniques and applications*. John Wiley & Sons, 2019.

[69] RC Jaklevic, J Lambe, JE Mercereau, and AH Silver. Macroscopic quantum interference in superconductors. *Physical Review*, 140(5A):A1628, 1965.

[70] Shigeji Fujita, Kei Ito, and Salvador Godoy. *Quantum theory of conducting matter: superconductivity*. Springer Science & Business Media, 2010.

[71] John Clarke and Alex I Braginski. *The SQUID handbook: Applications of SQUIDs and SQUID systems*. John Wiley & Sons, 2006.

[72] M Sawicki, W Stefanowicz, and A Ney. Sensitive SQUID magnetometry for studying nanomagnetism. *Semiconductor Science and Technology*, 26(6):064006, 2011.

[73] Lukas Spree, Fupin Liu, Volker Neu, Marco Rosenkranz, Georgios Velkos, Yaofeng Wang, Sandra Schiemenz, Jan Dreiser, Pierluigi Gargiani, Manuel Valvidares, et al. Robust Single Molecule Magnet Monolayers on Graphene and Graphite with Magnetic Hysteresis up to 28 K. *Advanced Functional Materials*, page 2105516, 2021.

[74] Matias Urdampilleta, Svetlana Klayatskaya, Mario Ruben, and Wolfgang Wernsdorfer. Magnetic interaction between a radical spin and a single-molecule magnet in a molecular spin-valve. *ACS nano*, 9(4):4458–4464, 2015.

[75] Ryo Nakanishi, Jyunya Satoh, Keiichi Katoh, Haitao Zhang, Brian K Breedlove, Masahiko Nishijima, Yusuke Nakanishi, Haruka Omachi, Hisanori Shinohara, and Masahiro Yamashita. $DySc_2N@C_{80}$ single-molecule magnetic metallofullerene encapsulated in a single-walled carbon nanotube. *Journal of the American Chemical Society*, 140(35):10955–10959, 2018.

[76] Stanislav M Avdoshenko, Fabian Fritz, Christin Schlesier, Aram Kostanyan, Jan Dreiser, Martina Luysberg, Alexey A Popov, Carola Meyer, and Rasmus Westerström. Partial magnetic ordering in one-dimensional arrays of endofullerene single-molecule magnet peapods. *Nanoscale*, 10(38):18153–18160, 2018.

Scientific publications

5.1 Author contributions

Paper I: Magnetic hysteresis in self-assembled monolayers of Dy-fullerene single molecule magnets on gold

I participated in the synchrotron measurements, initial data analysis and discussing the manuscript.

Paper II: Substrate-Independent Magnetic Bistability in Monolayers of the Single-Molecule Magnet $Dy_2ScN@C_{80}$ on Metals and Insulators

I participated in the synchrotron measurements, initial data analysis and discussing the manuscript.

Paper III: Controlled Oxidation and Self-Passivation of Bimetallic Magnetic FeCr and FeMn Aerosol Nanoparticles

I performed the SQUID magnetic measurements, provided the analysis and description of the data, wrote the magnetism part and discussed the manuscript.

Paper IV: Large exchange bias in Cr substituted Fe_3O_4 nanoparticles with FeO subdomains

I performed the XPS, XAS, SQUID measurements, did the subsequent analysis, performed the simulations and drafted the manuscript.

Paper v: Cr-substituted Fe_3O_4 nanoparticles: The role of particle size on the formation of Fe_xO subdomains and the emergence of exchange bias

I performed the magnetic measurements, the analysis and drafted the manuscript.

Paper vi: Nanoscale X-ray Study of Self-Assembled Magnetic Nanochains

I performed the STXM measurements and the analysis, participated in the PEEM measurements and did the analysis and contributed to the manuscript.

Printed by Media-Tryck, Lund 2021 NORDIC SWAN ECOLABEL 3041 0903

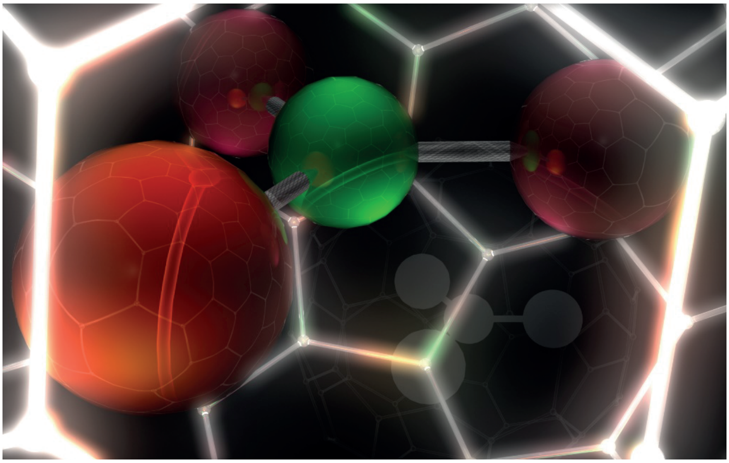

LUND
UNIVERSITY

Division of Synchrotron Radiation Research
Department of Physics
Faculty of Science
Lund University,
ISBN 978-91-8039-110-8